

International Journal of Innovations in Science & Technology

Volume 2
Issue 3



1. Flood Inundation Mapping using Multi-temporal Datasets
2. Appraisal of Trans Indus, Marwat-Khisor and Bhattani Ranges Thrusting through Geo-spatial Techniques
3. River Profile Modeling Through Surface Deformation Using RS/GIS, A Case Study Swat River
4. Generation of Digital Surface Model (DSM) USING UAV/ QUADCOPTER
5. EVALUATING FOCAL MECHANISM OF SEPTEMBER 24, 2013 AWARAM EARTHQUAKE WITH GEOSPATIAL TECHNIQUES

Journal.50sea.com



Prof Dr. Ali Iqtadar Mirza

Chief Editor

International Journal of Innovations in Science and Technology

Abstracting and Indexing



Recognized Journal



TOGETHER WE REACH THE GOAL



Instructions for Authors

The editorial board encourages and welcome true researches, laboratory experiments and real time field observations to get published in IJIST. The authors are advised to prepare their manuscript according to the template of IJIST.

Please see the checklist before submitting your manuscript to IJIST.

- The manuscript is prepared according to the template of IJIST.
- Symbols and names are used according to international standards.
- Page no and Line no are adjusted on the manuscript.
- Figure and Table are clearly cited.
- Author names and their affiliation are typed clearly.
- There is no any limit to the length of manuscript.
- Abstract is comprised of 250 words.
- Author's contribution and the statement narrating no of conflict of interest is mentioned in the end.
- Each Figure and Table is numbered and cited in the text.
- Spelling and English grammar is checked.
- It is "Open Access" journal that publish articles on payment of publishing fee by authors or by their institutions.
- All the articles are published under Creative Common License CC-BY therefore, authors mush agree with same license.

Aims and Scopes

The authors are advised to submit their manuscript in accordance with disciplines as below:

- Administrative Science
- Agriculture/Forestry
- Climatology
- Criminology
- Development Study
- Environment
- GIS
- Geography
- Meteorology
- Physics
- Remote Sensing
- Social Science
- Urban Planning
- Economics
- Chemistry
- Bio-Chemistry
- Computer Science

Peer Review Process

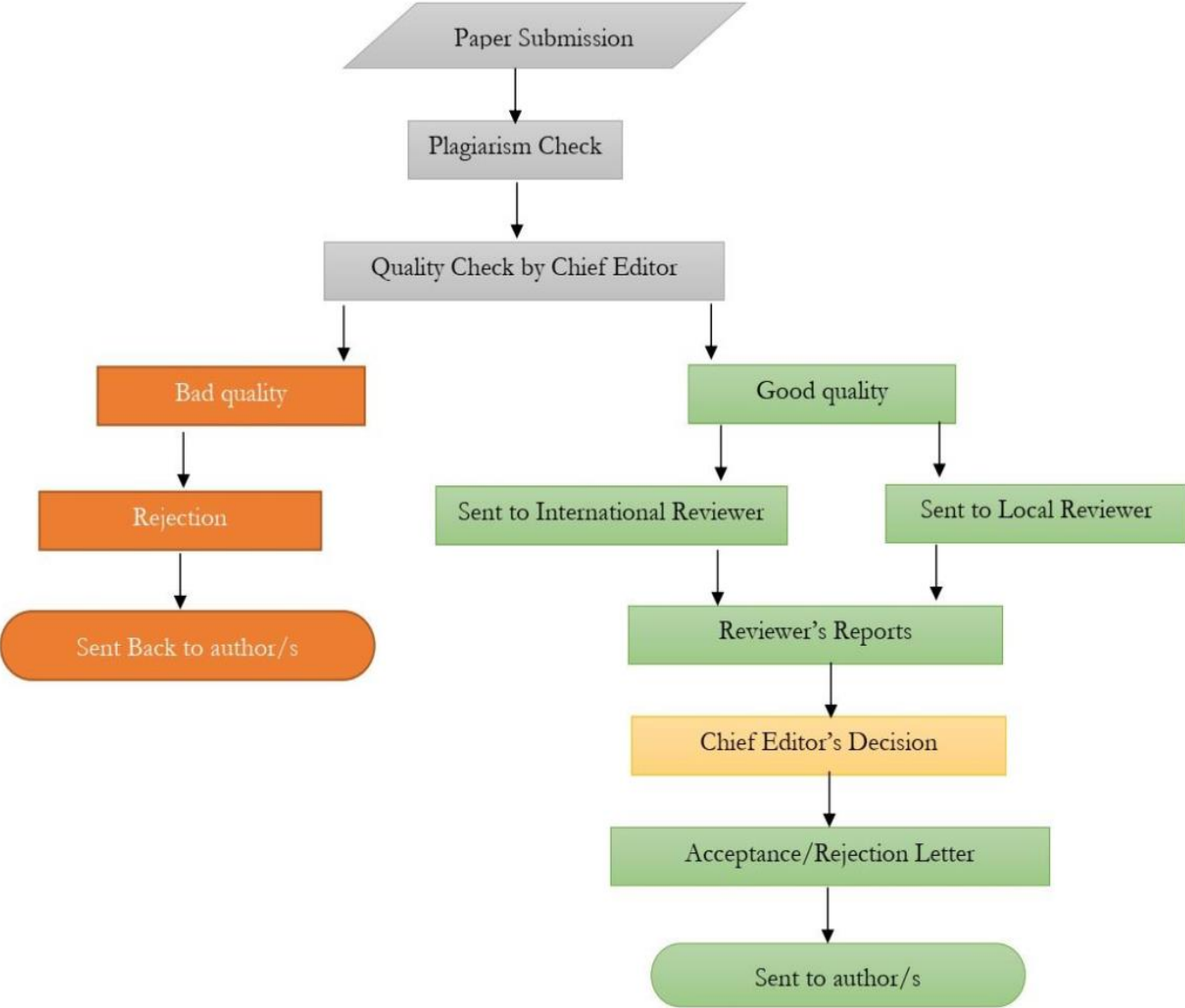


Table of Contents

**International Journal of Innovations in Science & Technology
(IJIST)**

ISSN 2618-1630

V2-I3 | September 2020

Sr No	Items	Page No.
1.	Flood Inundation Mapping using Multi-temporal Datasets	61-67
2.	Appraisal of Trans Indus, Marwat-Khisor and Bhattani Ranges Thrusting through Geo-spatial Techniques	68-74
3.	River Profile Modeling Through Surface Deformation Using RS/GIS, A Case Study Swat River	75-88
4.	Generation of Digital Surface Model (DSM) USING UAV/ QUADCOPTER	89-107
5.	Evaluating Focal Mechanism Of September 24, 2013 Awaran Earthquake With Geospatial Techniques	108-125



Flood Inundation Mapping using Multi-temporal Datasets

Syed Amer Mahmood¹, Saira Batool², Areeba Amer³, Mareena Khurshid⁴, Muhammad Shahzad¹,

¹ Department of Space Science University of the Punjab Lahore.

² Centre For Integrated Mountain Research (CIMR) University of the Punjab Lahore.

³ College of Earth & Environmental Sciences (CEES) University of the Punjab Lahore.

⁴ Department of Geography University of the Punjab Lahore.

* Correspondence: Areeba Amer and Email : Areebainspace@gmail.com

Citation | Mahmood.S.A, Batool.S, Amer.A, Khursheed.M, Shahzad.M, "Flood Inundation Mapping using Multi-temporal Datasets" International Journal of Innovations in Science & Technology, 2020 Vol 2 Issue 3 PP 61-67

Received | July 19, 2020; Revised | Aug 16, 2020; Accepted | Aug 18, 2020; Published | Aug 19, 2020.

Abstract.

Floods are considered the most frequent natural catastrophic events, which effect the human lives and infrastructure. Flooding causes tremendous loss of life and property every year. We used satellite imagery to map flood inundation in Jehlum river for the both pre and post flood scenarios and classified it into major landuse including vegetation, water body, buildup land and the bare soil. The results show that about 40% area was agricultural land, 29% was bare soil, 16% was build up land and 12% area was noted as water body. The categorization of the post flood areas, showed that flood has destroyed the buildup and agriculture lands. The superimposition proposed that agricultural land was 43% before the flood which reduced up to 31%, the normal flow of water was 12% before flood which was increased up to 33%, build up area and bare soil was also decreased up to 10% and 25% respectively. Remote sensing and GIS proved efficient in convergence of optimistic results.

Keywords: Natural Disasters, Pre and Post Flood, Landuse, Land cover.

Introduction

Natural disasters are common phenomenon occurring worldwide. Flood is one of the most destructive [1], devastating and frequently widespread calamity among different types of natural disasters [2,3]. Almost \$500 billion is lost every year in rehabilitation of natural disasters caused by climate changes. Particularly, floods being the most frequent natural catastrophic event, have affected human lives and infrastructure. Flooding causes tremendous loss of life and property every year [3]. According to the directive of European Union (EU), flood is defined as an interim arrangement of water on a piece of land which is normally devoid of water. River flood is a phenomenon usually occurs when water level of a river rises beyond its capacity due to rainfall and melting snow or ice. Thus, rivers overflow during monsoon season causing extensive floods. The Himalayan region of India was

spotted with unrivalled flooding in the last few years, such as flood of Ganga in 2010, flood of Brahmaputra 2012 and Jhelum floods in 2014.

The floods leave long term effects on regions which witness downpour for a long period or tremendous water flows from the rivers. Flood extent is determined through data collected by optical and radar satellites. The data which is collected through in-situ collection can be inadequate, impractical and expensive. Aerial imagery can prove expensive and provide data which have limited spatial and temporal resolution. Moreover, the height of water is determined through gauge station but gauge station is unable to measure extent of flood. Whereas, the extent of flood can be determined in frequent intervals of time through the satellite imagery over a vast geographical extent [4].

The effects of floods can be minimized and reduced through proper redeem, relief and allocation of resources for rehabilitation and retrieval of destructed land but floods cannot be avoided. The first available satellite imagery is acquired for the collection of data needed to map the lands under floods. Satellite imageries are extensively used to evaluate temporal changes worldwide due to their compendious coverage. In order to establish a quick response plan and to reduce the natural disasters, it is very important to organize accurate inundation mapping in frequent intervals of time [5,6,7].

Ground surveys were considered a major source of information but these are now time consuming and wastage of resources and cannot persuade a quick response when a natural calamity spreads to a large scale. Moreover, data obtained through aerial surveillance can be inaccurate in some extreme atmospheric conditions, and the density of gauging stations is inadequate in various scenarios [8]. The Satellite Remote Sensing (SRS) is commonly used [9] due to widespread accessibility in terms of time and cost [10]. Progress of floods can be monitored through multi-temporal images.

Microwave remote sensing provides real time earth observations regardless of weather conditions and indispensable for observation of flood because of its capacity. Various techniques have been devised for mapping inundation using multi-temporal satellite images. Normalized Difference Water Index (NDWI) generated by Mc Feeters [11] is an indices to map water bodies, which provides effective results for inundated lands [12]. For example, Wang et al. [13] initiated Otsu's algorithm for selection of water bodies automatically. The effectiveness of Otsu's algorithm is reduced because of the mixed pixels in satellite images and recurrent illumination differences, especially for some complicated sequences.

The extent of flood is determined from the change analysis using segmentation techniques. Rahman et al. [14], combined the multi-temporal NDWI images into single file and processed it to analyze through Principal Component Analysis (PCA). All these techniques are based on spectral responses and the capacity of each method can fluctuate with changing of spectral features, these methods are applied to different cases by the use of different sensors.

Chen et al. [15] devised a method to monitor water surface using spectro-temporal images. Moderate Resolution Imaging Spectroradiometer (MODIS) data is considered adequate and valid to over large extents using unsupervised classification. However, the statistical equality depends upon uni-dimensional features, which are basically the avenue of temporally adjoining pixels. Moreover, the performance of MODIS data has been reduced due to low spatial resolution in spatial dimension.

This study aims at determining the flood extent using freely available satellite images. It also aims at investigation of rehabilitation activities in post flood scenarios.

Material and Methods.

Investigation site.

Verinag spring is the starting point of Jhelum River located in south eastern Kashmir's valley adjacent to PirPanjal situated in India. The river passes through Srinagar and through stony barriers of Wular-Lake before entering the territory of Pakistan [16]. River Jhelum flows along the district Jhelum and passes by south of Pakistan. Jhelum is located at west bank of river of Punjab and it was discovered by Alexander in 325 BC. It is controlled by snow melt from glaciers of Kashmir in spring season. This snowmelt is the main supplier of water in this river. The water level in river substantially rises in monsoon season from June to September due to heavy rainfall which causes heavy water flow into the river. The water discharge and flow speed in Jhelum river exceeds upto 1,000,000 cubic per second. Due to minor rainfall in winter season, the water level of river falls substantially. Thus, water level of river Jhelum is high in summer and low in winter season. The river launch into Punjab province through Jhelum district and then flow towards the plain areas of Punjab and prolong towards Sagar doab [17].

The river passes through Jhelum, Muzaffarabad, Khushab, Mandi Bahauddin, Jhang, Malakwal, Multan, Muzaffargarh, and Sahiwal [9]. The annual average flow of river can be calculated through the combination of daily average flows of the river. The average flow recorded on annual basis is about 12 MAF i.e., with 3.65 MAF in Kharif and Rabi seasons respectively and 8 MAF in season [10].

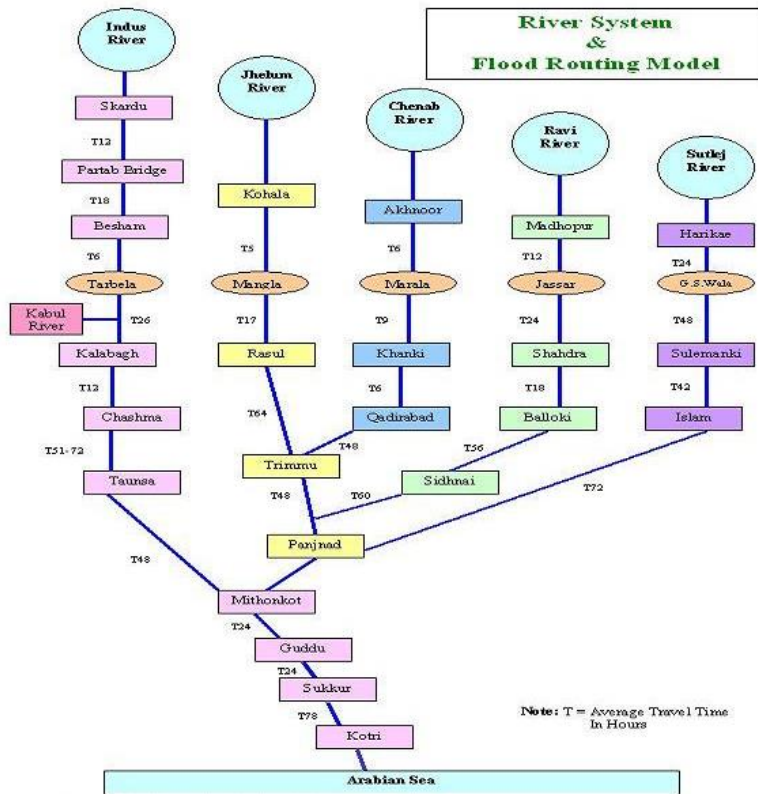


Figure 1. Spatial location of Jhelum River

Source: <https://www.pakimag.com/misc/pakistan-river-system-map-with-head-works.html/attachment/river-map-pakistan>

Material and methods.

USGS website was used to obtain Landsat-8 images which are freely available to download. Flood alluvion data for the dates August 25, 2014 (pre flood) and September 10, 2014(post flood) was downloaded from USGS website. The downloaded images were composed of 11 spectral bands which were confined through layer stack utility embedded in Erdas Imagine. Fluctuations in sensor's functionality causes geometric distortions which were inspected and catered in Erdas Image 9.2 in order to make data error free. Supervised classification was applied to classify satellite images into major classes as buildup area, bare soil and the water body. Subsetting was performed to extract the desired area from large datasets using masking algorithm in Arc GIS10.1. Sub setting is performed to increase the processing speed which saves time and lead to the better performance of work stations. Classified raster datasets were converted to polygons and integrated in order to measure the extent of systematic water flow in comparison to the extent of flood inundation.

Result and discussion.

The classified images were categorized into major groups which include agricultural land, built up, bare soil and the water body. Urban areas include the constructive structures of residents such as apartments, educational institutes, public buildings and commercial markets etc. The major crop plants across the fields include the agricultural land.

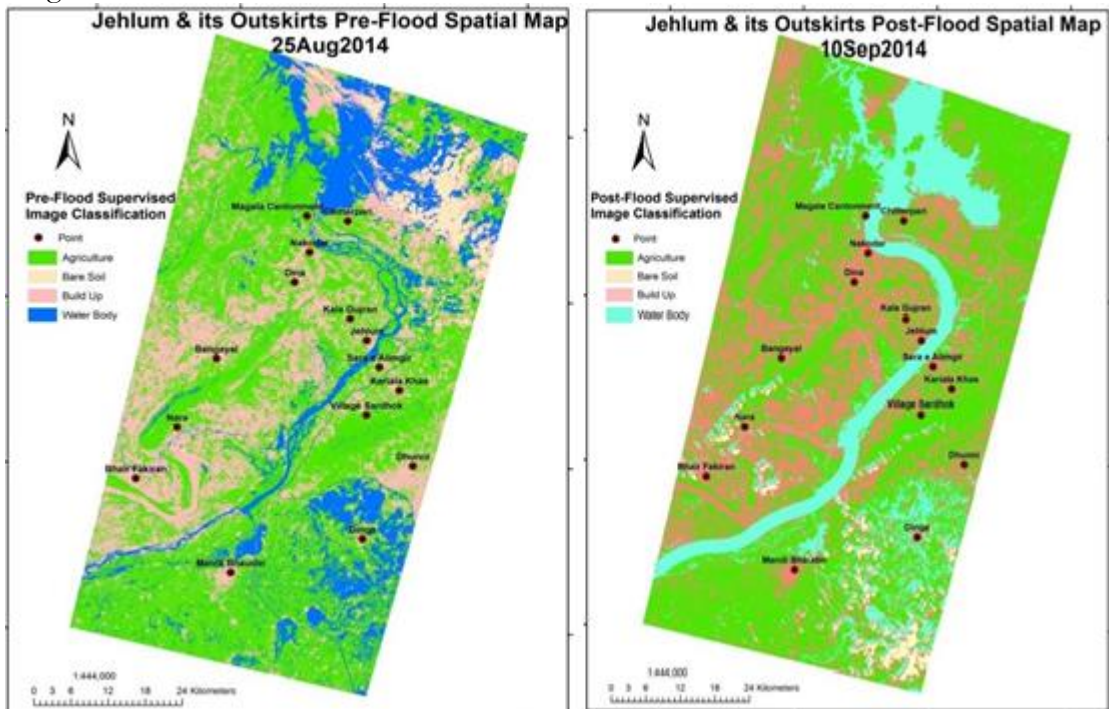


Figure 2. Pre and Post flood classified maps of river Jhelum.

Table 1. Statistics before flood.

Agriculture	Bare soil	Build up area	Water body
-------------	-----------	---------------	------------

2732 SqKm	1464SqKm	819 SqKm	196SqKm
-----------	----------	----------	---------

The statistics describe that about 40% area was agricultural land and 29% was bare soil and 16% was build up land and 12% water body was noted. The categorization of the post flood areas, showed that flood has destroyed the buildup and agriculture area. The post flood classified image is shown below.

Table 2 Statistics in Post-flood conditions.

Agriculture	Bare soil	Build up area	Water body
2511 SqKm	1325 SqKm	409 SqKm	1193 SqKm

Pre and post flood analysis

The following results were obtained by superimposition of the pre and post flood categorized images for flood inundation mapping. The superimposition proposed that agricultural land was 43% before the flood which reduced up to 31% , the normal flow of water was 12% before flood which was increased up to 33%, build up area and bare soil was also decreased up to 10% and 25% respectively.

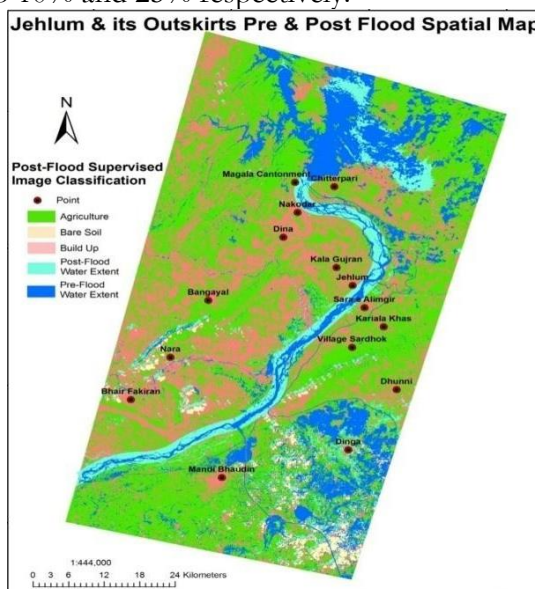


Figure 3. Pre and post flood classified superimposed map.

Aftermath of flood

Flood being, a natural calamity, has hit many areas indiscriminately. The geography of the Jehlum and its outskirts was observed interrupted badly in post flood situations. The flood caused life losses and demolishing of infrastructure effecting the economy badly. The rehabilitation and reconstruction of these demolished built-up areas require long time and amount.

Flood affected the study site and a large variety of hazardous substances and chemicals were transported and entered in to the study site. It caused various kinds of diseases but on the crop, productivity was enhanced up to many folds in upcoming years in post flood situations.

Agronomist consider floods a sign of goodness because flood water transport rich minerals which are the best for productivity. The overall flora and fauna of this region was

affected badly. The observations showed that transportation system of the study area was destroyed by the flood. It also destroyed the residential structures including schools, industrial zone, infrastructure and sanitation facilities.

Flood proved to be vulnerable for the residents of study site who lost their lives and property. Flood also had psychodynamic effects in a community. Economic development was also reduced by flood. Moreover, the destruction by flood also resulted in the mass migration.

Author's Contribution. All authors contributed equally.

Conflict of interest. Authors declare no conflict of interest for publishing this manuscript in IJIST.

Project details. Nil

REFERENCES

1. Ahmed, M.S., Eldin, E., Abdelkawy, F., Tarek, M.A., Speckle noise reduction in SAR images using adaptive morphological filter. 2010 10th International Conference on Intelligent Systems Design and Applications. Pp: 260-265, 2011.
2. Cutter SL, Barnes L, Berry M, Burton C, Evans E, Tate E, Webb J. A place-based model for understanding community resilience to natural disasters. *Global environmental change*. VOL 18, issue 4, pp :598-606, 2008.
3. C. M. Bhatt*, G. Srinivasa Rao, Asiya Begum, P. Manjusree, S. V. S. P. Sharma, L. Prasanna and V. Bhanumurthy "Satellite images for extraction of flood disaster footprints and assessing the disaster impact: Brahmaputra floods of June–July 2012, Assam India", Vol 104, issue 12, pp: 1692 – 1700, 2013.
4. Huang et.al. *Geomatics Natural Hazards Risk, GEOMAT NAT HAZ RISK*, Vol 7, issue 2, pp. 747-763, 2016,
5. Huang et.al. *Geomatics Natural Hazards Risk, GEOMAT NAT HAZ RISK*, Vol 12, issue 1, pp. 384-401, 2021.
6. Bhatt, C. M., Rao, G. S., Farooq, M., Manjusree, P., Shukla, A., Sharma, S. V. S. P., Kulkarni, S. S., Begum, A., Bhanumurthy, V., Diwakar, P. G., Dadhwal, V.K. Satellite-based assessment of the catastrophic Jhelum floods of September 2014, Jammu & Kashmir, India. Vol 8, Pp: 309- 327, 2017.
7. O'Keefe, P.; Westgate, K.; Wisner, B. Taking the naturalness out of natural disasters. *Nature*, Vol 260, pp: 566–567, 1976.
8. Sanyal, J.; Lu, X.X. Application of remote sensing in flood management with special reference to monsoon Asia: A review. *Nat. Hazards*, Vol 33, pp: 283–301, 2004.
9. Berz, G.; Kron, W.; Loster, T.; Rauch, E.; Schimetschek, J.; Schmieder, J.; Siebert, A.; Smolka, A.; Wirtz, A. World map of natural hazards—A global view of the distribution and intensity of significant exposures. *Nat. Hazards* Vol 23, pp: 443–465, 2001.
10. Akıncı, H.; Erdoğan, S. Designing a flood forecasting and inundation-mapping system integrated with spatial data infrastructures for Turkey. *Nat. Hazards*, Vol 71, pp: 895–911, 2014.
11. Smith, L.C. Satellite remote sensing of river inundation area, stage, and discharge: A review. *Hydrol. Process.* Vol 11, pp: 1427–1439, 1997.

12. Brivio, P.A.; Colombo, R.; Maggi, M.; Tomasoni, R. Integration of remote sensing data and GIS for accurate mapping of flooded areas. *Int. J. Remote Sens.* Vol 23, pp: 429–441, 2002.
13. Wang, Y.; Colby, J.D.; Mulcahy, K.A. An efficient method for mapping flood extent in a coastal floodplain using Landsat TM and DEM data. *Int. J. Remote Sens.* Vol 23, pp: 3681–3696, 2002.
14. Rahman, M.S.; Di, L. The state of the art of spaceborne remote sensing in flood management. *Nat. Hazards* Vol85, pp: 1223–1248, 2017.
15. Li, L.; Chen, Y.; Yu, X.; Liu, R.; Huang, C. Sub-pixel flood inundation mapping from multispectral remotely sensed images based on discrete particle swarm optimization. *ISPRS J. Photogramm. Remote Sens.* Vol 101, pp: 10–21, 2015.
16. Asgary, A., Anjum, M. I., &Azimi, N. Disaster recovery and business continuity after the 2010 flood in Pakistan: Case of small businesses. *International journal of disaster risk reduction*, Vol 2, pp: 46-56, 2012.
17. Aparna, N., Ramani, A. V., &Nagaraja, R. Risk management support through India Remote Sensing Satellites. *The International Archives of Photogrammetry, Remote Sensing and Spatial Information Sciences*, Vol 40, issue 8,pp: 1, 2014.



Copyright © by authors and 50Sea. This work is licensed under Creative Commons Attribution 4.0 International License.



Appraisal of Trans Indus, Marwat-Khisor and Bhattani Ranges Thrusting through Geo-spatial Techniques

Iftekhhar Hussain¹, Syed Amer Mahmood¹, Saira Batool², Areeba Amer³, Mareena Khurshid⁴, Imran Saddique Kaukab¹,

¹Department of Space Science University of the Punjab Lahore.

²Centre for Integrated Mountain Research (CIMR) University of the Punjab Lahore.

³College of Earth & Environmental Sciences (CEES) University of the Punjab Lahore.

⁴Department of Geography University of the Punjab Lahore.

* Correspondence: Saira Batool and Email: sairabnaqvi5@gmail.com

Citation | Azeemi. I, Mahmood .S.A, Batool.S,Amer.A, Khurshheed.M, Kaukab I.S, Appraisal of Trans Indus, Marwat-Khisor And Bhattani Ranges Thrusting Through Geo-Spatial Techniques, International journal of Innovations in Science & Technology, 2020 Vol 2 Issue 3 PP 68-74

Received | July 22, 2020; Revised | Aug 15, 2020; Accepted | Aug 16, 2020; Published | Aug 20, 2020.

Abstract.

Himalayan mountain belt was created by the Indo–Eurasian collision. The length of this seismically active mountain belt is almost 2500 km. Southern partition of this zone is marked by the main frontal thrust. We computed the isobase, relative relief, incision, vertical dissection and drainage density maps of the study site. Drainage density is inversely proportional to the rest of computed parameters. Drainage density is less where the incision/deep cutting is high. Pezu and north western parts of the study site are observed vulnerable to tectonic activity and high risks. These sites are the adjoining parts of active faults. The rates of morphological changes and the combination of stripping processes are determined through Surface dynamics maps (SDM). Although it is a handy tool used to evaluate erosion conditions of sags or sub basins. Remote sensing and GIS techniques proved efficient for appraisal of thrust in Marwat Kishore and Bhattani ranges.

Keywords: Thrusting, Relative Relief, Isobase coding, Drainage density.

Introduction

The Himalayan mountain belt was created by the Indo–Eurasian collision. The length of this seismically active mountain belt is almost 2500 km. Southern partition of this zone is marked by the Main Frontal Thrust (MFT) [1,2]. The growth and development of MFT is necessary to unwind the process of deformation of mountain belts and preparation of major jeopardy of future related to active tectonics of these belts. The data gained through geodesy suggests that the Indian plate move at the rate of 35mm/year in northwestern boundary while 38mm/year in northeastern direction [3]. According to Lave and Avouac most of the Himalayan deformations were recorded in MFT [4]. The deformation was deliberated 9 ± 3 mm/year in the northwestern, 21 ± 1.5 mm/year in

central and 23.4 ± 6.2 mm/year in eastern Himalayas [4,5,6,7,8]. The MFT is a youngest frontal thrust and a narrow region located in the central and eastern Himalayas which has a high degree of cross-section; however, a low degree of cross-sectional taper is located in the western Himalayas which is 100 km wide [9,10]. Moreover, the Indian plate rotates in an anticlockwise direction shifting the trend from NW-SE of central and eastern Himalayas to NE-SW located in Pakistan [11]. Himalayan arc is mapped in Figure 1.

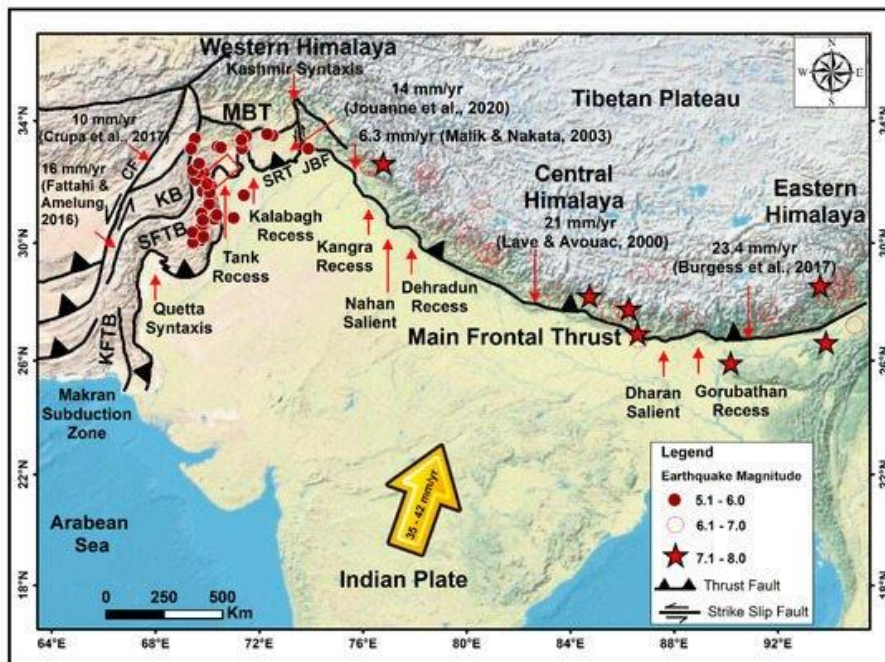


Figure 1. Himalayan arc observed through satellite imagery

Source:<https://www.mdpi.com/2072-4292/12/20/3362/htm>.

Several historic earthquakes which had a magnitude higher than seven were associated with the MFT. These earthquakes had the ability to rupture the surface of land. The Himalayas located in the north of Pakistan elongates from Jhelum fault in east to western Ophiolite Belt. The main frontal thrust of Western Himalia is classified as salt Indus ranges and trans Indus ranges.

According to geodetic data, southward translation of western salt rang is 10mm/year and central salt range is 5mm/year. However, Kalabagh fault zone displaced the Trans Indus Range (TIR) at the rate of 5.3 mm/year. Blisniuk et al. and Abir et al. [12] suggested that the basal detachment is formed along the MFT by the salt range in the west of Himalayas. Chronostratigraphic studies proposed that western Himalayas are youngest collisional zone which is deforming actively.

The trans indus ranges are further sub-divided into the Surghar, Manzai, Marwat–Khisor, and Bhattani Ranges (Figure 2). These ranges portray condensational deformation and show lateral structural variations along the salient faults. Moreover, transpersonal deformation occurred along strike–slip faults [10]. The Kalabagh and Tank faults are separated by Marwat–Khisor salient in the TIR.

The main objective of this study is to determine the deformation pattern, displacement rate and landscape development relative to active tectonics of western Himalayans.

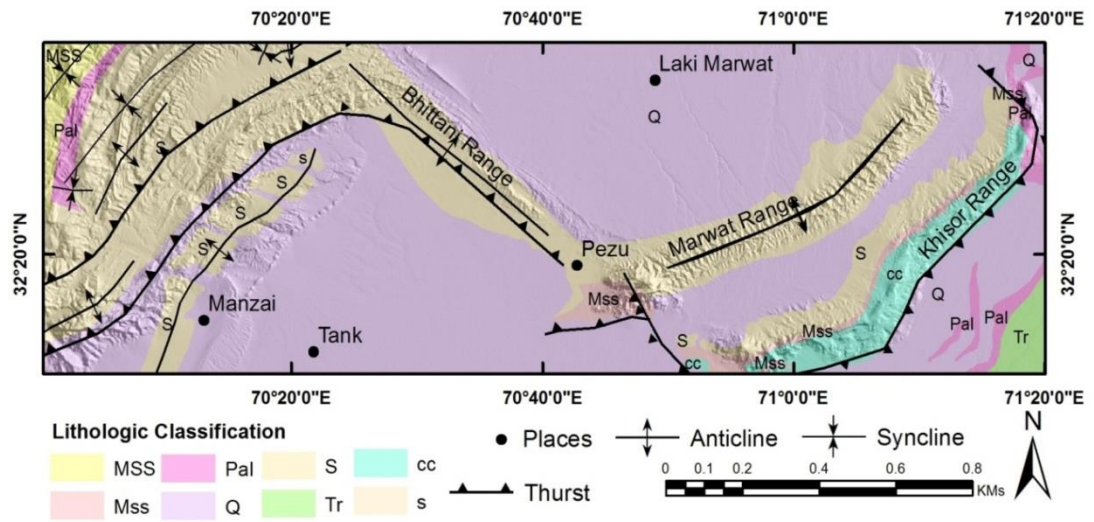


Figure 2. Fault setting in the study stie.

MATERIALS AND METHODS

Study Area

The area under study covers about 7850 square kilometers of Bannu, Kalabagh, Lakki Marwat, Pezu, Tank and D.I.Khan (Figure 3).The study area is situated about 200 Kilometers away from Peshawar towards south-southwest.

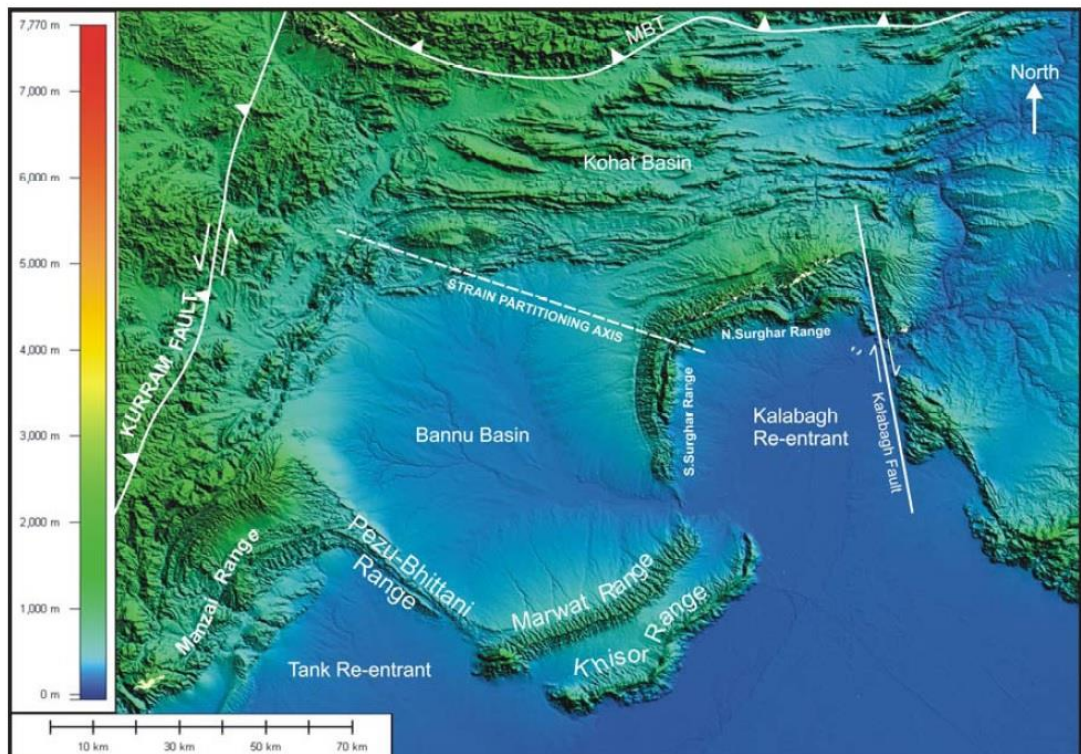


Figure 3. Ranges present in the study site

Data Acquisition and Processing

Data was obtained through geological fieldwork for geological mapping of trans Indus ranges and geological cross-sections were established to comprehend geometry and structure of Trans Indus range. Two types of data were used for active tectonic mapping which include vector data and Shuttle Radar Topographic Mission (SRTM) Digital Elevation Model (DEM) [13].

Digital Elevation Model (DEM)

DEMs are helpful in determining geographic information based on digital relief maps. However, DSM (Digital Surface Model) was used in landscape mapping and city modeling.

Longitudinal River Profile analysis

A flow direction of any topographic region is determined through D8 algorithm. In this method, flow from one pixel to its neighboring pixels is tracked. D8 flow grid is generated from a depression less DEM. This method is used to determine flow from flat to reducing valleys. Incision determine the nature of geology, soft rocks determine erosion while hard rocks lead to vertical cutting/incision. Relative relief describes the variation in slop, high relative relief leads to gentle slopes while low relative relief describes the steep slopes. Drainage density was computed using hydrological tools on digital elevation model, where large drainage density leads to rough topography.

Concavity and steepness

Stream power model is used to estimate the drainage area and channel gradient (Whipple and Kirby, 2001; Kerby and Howard 1983):

$$dz / dt = U(x, t) - KA^m S^n \text{ Eq. 1}$$

Where dz/dt is the rate of change in variation of channel’s elevation, U determine the rate of uplift in rock, A describe the area of drainage, S is the slope of each channel, K is the coefficient of erosion and m and n describes the hydrology and hydraulic geometry respectively. The value of dz/dt is zero in steady state conditions. To compute the slope of channel, following expression is used,

$$S = (U / K)^{1/n} A^{-(m/n)} \text{ Eq. 2}$$

Equation 2 describes a relationship between the area of drainage line and the channel gradient which is commonly observed in natural conditions.

$$S = k_s A^{-\theta} \text{ Eq. 3}$$

Here the factor (U/K)1/n determine the steepness, ks and m/n is the concavity. We simply applied log on both sides of equation 3,

$$\log S = -\theta \log A + \log k_s \text{ Eq. 4}$$

Where θ determine the concavity and K_s is the steepness which may be computed by regression in log plot of slope and drainage area.

RESULTS AND DISCUSSIONS

Hack gradient index and geomorphic indices were analyzed in the study site in order to interpret relative uplifting, regional topography and crustal slanting within the region. The concavity (θ) and steepness (ks) indices were calculated using stream power law by establishing stream longitudinal profile analysis on 116 small and large channels which were extracted through the SRTM DEM. We applied regression models to active tectonic signals from streams in order to determine concavity indices and steepness. The steepness index values fluctuate between high or low concavity. Spatially inconstant lithologies, or spatially variable relative bedrock uplift rates causes such a fluctuating zone.

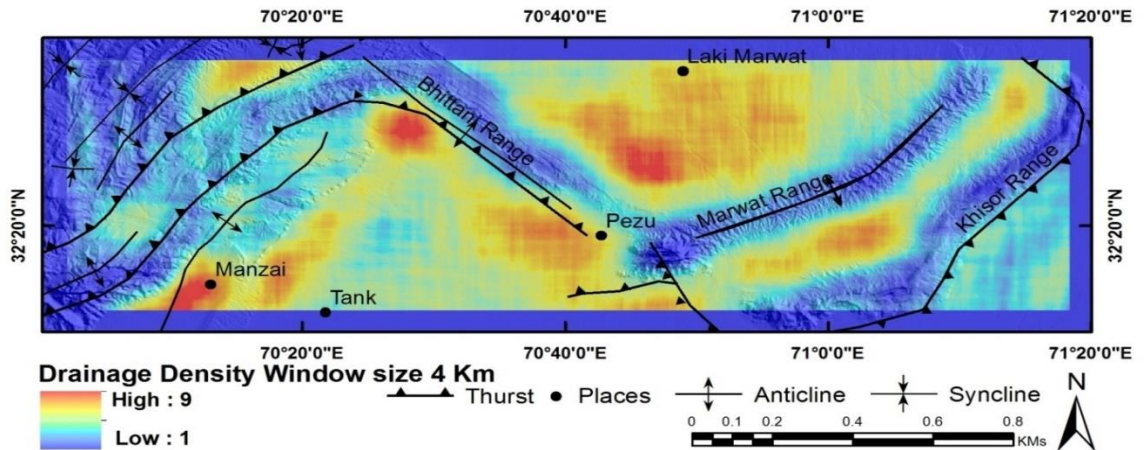


Figure 4. Drainage Density Map at 4Km window.

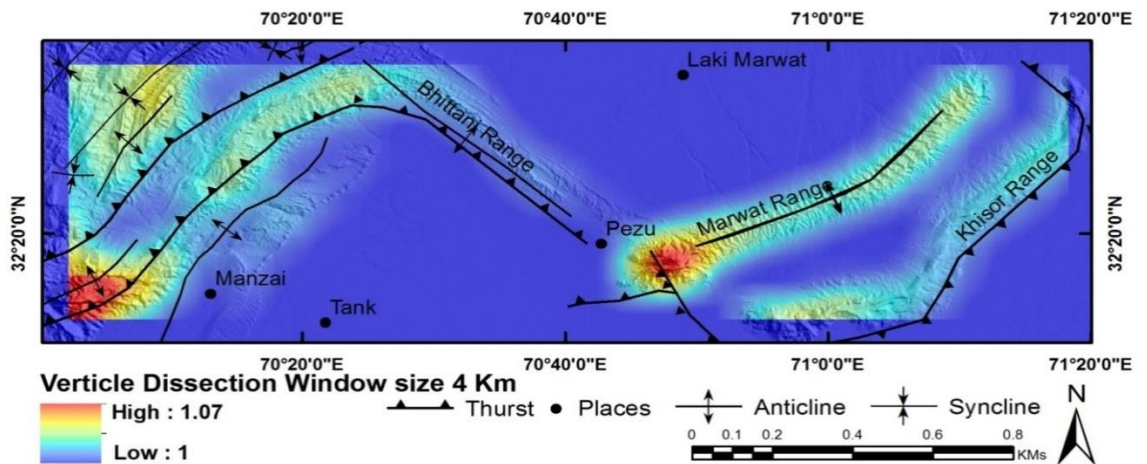


Figure 5. Vertical dissection window at 4Km window.

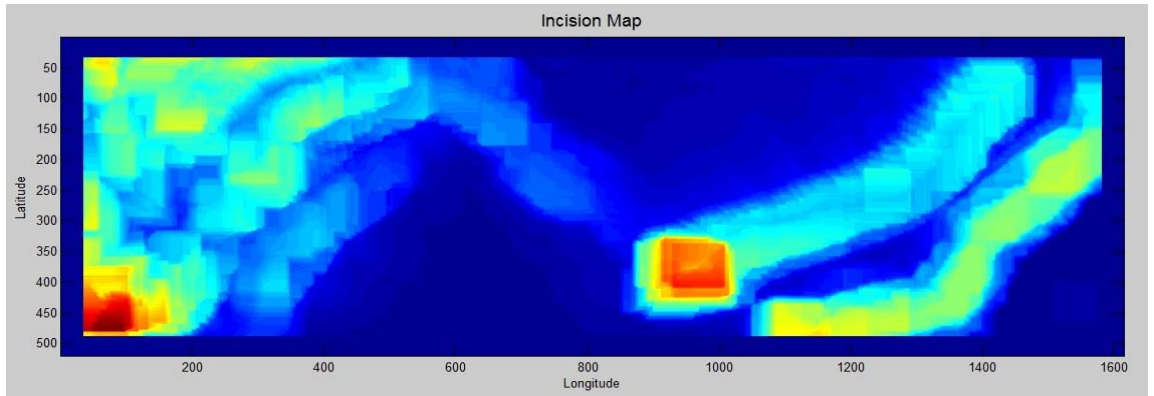


Figure 6. Incision Map at 4Km window.

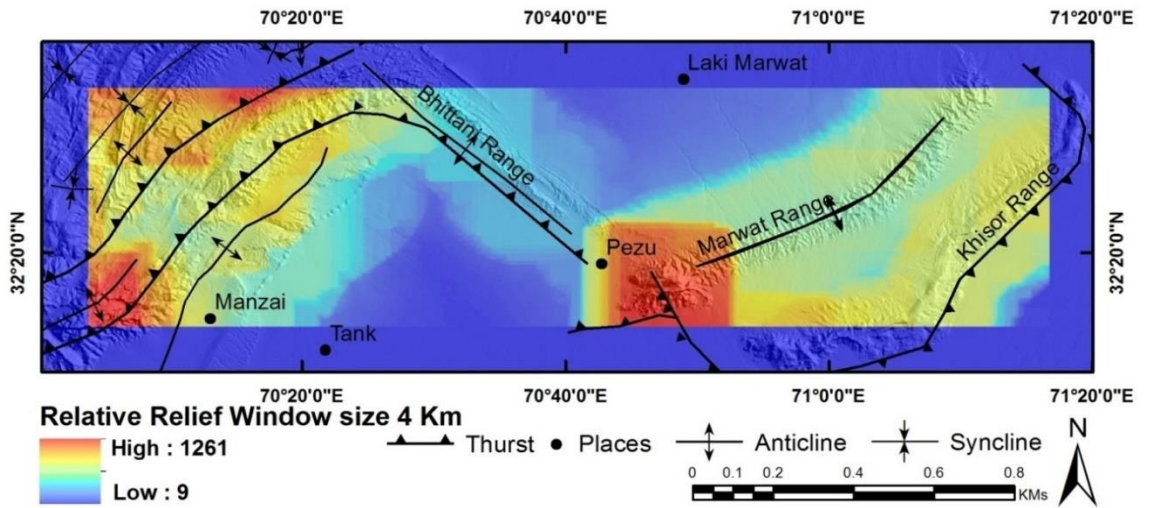


Figure 7. Relative Relief Map at 4Km window.

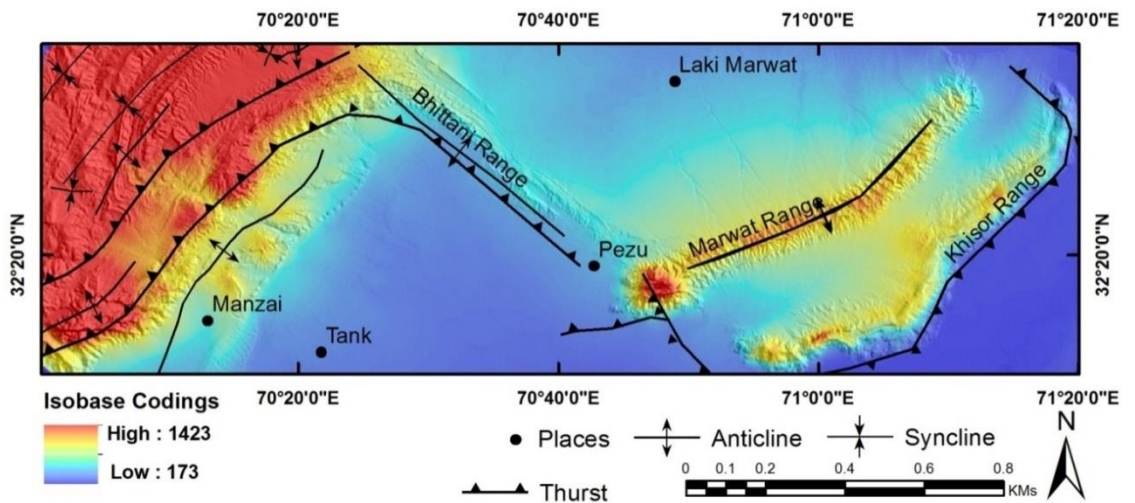


Figure 8. Isobase Coding Map at 4Km window.

Figures 4-8 determine the isobase, relative relief, incision, vertical dissection and drainage density maps of the study site. Drainage density is inversely proportional to the rest of computed parameters. Drainage density is less where the incision/deep cutting is high. Pezu and north western parts of the study site are observed vulnerable to tectonic activity and high risks. These sites are the adjoining parts of active faults.

The rates of morphological changes and the combination of stripping processes are determined through Surface dynamics maps (SDM). Although it is a handy tool used to evaluate erosion conditions of sags or sub basins. Differential erosion and neotectonics activity were found behind the uplift of study site due to abundant precipitation in summer as well as in winter and tectonic domination over climate and erosion.

Author's Contribution. All authors contributed equally.

Conflict of interest. Authors declare no conflict of interest for publishing this manuscript in IJIST.

Project details. NIL

REFERENCES

1. Abbott, L.D., Silver, E.A., Anderson, RS., Smith, R, Ingle J.C., Kling, S.A., Haig, n, Small, E. Galewsky, J" and Sliter, W., Measurement of tectonic surface uplift rate in a young collisional mountain belt: *Nature*, v. 385, pp: 501-507, 1997.
2. Ahnert, E, Functional relationships between denudation relief, and uplift in large mid-latitude basins: *American Journal of Science*, v. 268, p. 243-263, 1970.
3. Anderson, RS., Evolution of the Santa Cruz Mountains, California, through tectonic growth and geomorphic decay: *Journal of Geophysical Research*, v. 99, issue. B10, pp: 20161-20179, 1994.
4. Anderson, RS., and Humphrey, N.F, Quantitative Dynamic Stratigraphy: Englewood Cliffs, NJ, PrenticeHall, 1990, pp. 349-361.
5. Burbank, D. Rates of erosion and their implications for exhumation. *Mineralogical Magazine*, Vol 66, issue 1, pp: 25-52, 2002.
6. Blythe, Ann & Burbank, Douglas & Farley, K. & Fielding, Eric.. Structural and topographic evolution of the central Transverse Ranges, California, from apatite fission-track, (U-Th)/He and digital elevation model analyses. *Basin Research*. Vol 12, pp: 97-114, 2000.
7. L.L., and Lillie, RJ., ed., Tectonics and Geophysics of the Western Himalaya, Geological Society of Burbank, Geological society of America, Vol 232, pp: 176-210, 1989.
8. Burbank, D.W., and Beck, RA., Interactions of growing folds and coeval depositional systems: *Basin Research*, v. 8, issue 1, pp. 199-223.
9. Gomberg, J.S., Tectonic deformation in the New Madrid seismic zone; inferences from map view and cross sectional boundary element models: *Journal of Geophysical Research*, v. 98, p. 6639-6664, 1993.
10. Evans, I. S. Spatial Analysis in Geomorphology. Harper and Row, London, General geomorphometry, derivatives of altitude, and descriptive statistics. In: Chorley, R.J. (Eds.), 1972, pp. 17-90.
11. Strahler, A. N.: Quantitative analysis of watershed geomorphology. *Transactions of the American Geophysical Union* Vol 8, issue 6, pp: 913-920, 1957.
12. Strahler, A.N., "Hypsometric (area-altitude) analysis of erosional topography", *Geological Society America Bulletin*, Vol 63, issue 11, pp: 1117-1142, 1952.

13. Chen, Y.C., Sung, Q. and K.Y. Cheng, “Along-strike variations of morphotectonics features in the Western Foothills of Taiwan: Tectonic implications based on stream-gradient and hypsometric analysis”, *Geomorphology*, Vol 56, issue 1-2, pp: 109-137, 2003.



Copyright © by authors and 50Sea. This work is licensed under Creative Commons Attribution 4.0 International License.



River Profile Modeling Through Surface Deformation Using RS/GIS, A Case Study Swat River

Hafsa Amen¹, Syed Amer Mahmood¹, Saira Batool², Areeba Amer⁵, Mareena Khurshid³, Sadia Sadiq¹, Sajjad Ali Gill⁴

¹ Department of Space Science University of the Punjab Lahore.

² Centre for Integrated Mountain Research (CIMR) University of the Punjab Lahore.

³ Department of Geography University of the Punjab Lahore.

⁴ Department of Sports Science University of the Punjab Lahore.

⁵ College of Earth & Environmental Sciences (CEES) University of the Punjab Lahore.

* Correspondence: Marina Khursheed and Email : marinakhurshid@gmail.com

Citation | Amen.H, Mahmood.S.A, Batool.S, Amer.A, Khursheed.M, Sadiq.S, Gill S.A., ” River Profile Modeling Through Surface Deformation Using RS/GIS, A Case Study Swat River” International Journal of Innovations in Science & Technology, 2020 Vol 2 Issue 3 PP 75-88

Received | Aug 11, 2020; Revised | Sep 08, 2020; Accepted | Sep 09, 2020; Published | Sep 10, 2020.

Abstract.

The objective of this appraisal is to determine the feasibility of dam sites in Swat Valley and its peripheries (Northern Pakistan). We exploited SRTM DEM with a spatial resolution of 90m to extract various geomorphic indexes for the dam site feasibility. This research aims at pinpointing areas which can be opted for small dam constructions to overcome the electricity crisis in Pakistan to some extent to meet the national electricity needs. We exercised River profile analysis (RPA), D8 flow popular algorithm, Concavity, Steepness, and Hack-gradient methods to prepare interpolated maps for the Steepness index, Concavity index, Relative uplift rates, and other parameters like value zoom, vector zoom, surface zoom, density zoom, relief zoom and contour map. The drainage pattern of this area indicates that there are high relative uplift rates, erosion, steepness and concavity in NE, NW and SW. The DEM based RPA develops as much easier and faster approach to demarcate sites influenced by neotectonics.

Keywords: Natural Disasters, Pre and Post Flood, Landuse, Land cover.

Introduction

Flood risks in urban areas have been increased in recent years due to population growth and increased economic activities [1]. Flood risks should be identified, assessed and managed properly by using reliable and appropriate measures. Traditionally, the river stages and flood flows are modeled by using one dimensional hydrodynamic model due to their low cost and scarce field data requirement. Complex river and hydraulic systems such as bridge pier are efficiently represented by these models [1,2]. However, these models are not appropriate and accurate for representing the river stages and flood flows [3]. The 1D model can appropriately represent the river shapes. Chen et al. [4] determined that 1D hydrodynamic

models have some limitations and cannot represent the topography, river bathymetry and also inappropriate to represent the conditions of complex hydrodynamic river systems[5,6]. Therefore, the two- or three-dimensional models are proposed to overcome the limitations.

Although 2D and 3D models successfully represent the river processes, their precise application depends upon the accurate representation of river bathymetry [7]. The 2D and 3D models contain bathymetric data extracted by the cross sectional observation of elevations residing at the nodes of finite element mesh model [8,9,10]. Spatial bathymetric data has been used in many researches for the simulation of models. The ability of spatial prediction techniques to assume unmeasured area using discrete data defines the accuracy of bathymetric representation of 2D or 3D models[4,11,12]. These spatial prediction techniques include splines, Inverse Distance Weighting (IDW), triangulation, and Kriging [13]. The river topography cannot be predicted if there exists anisotropy in measured cross-sectional data of river systems. In order to generate missed data between cross sections, Beasley et al. introduced an algorithm [3]. This algorithm needs a cubic Hermite spline to produce a river bed which contains morphological characteristics[3,7,14,15].

Fluvial stage simulation of 2D and 3D model requires large amount of topographic and bathymetric data. In order to accurately predict unmeasured areas, appropriate interpolation methods are required. Morphodynamic models of river stage and sediment transportation requires hypsometry techniques to generate Digital Terrain Data (DTM) [8,16]. Dry areas of river can also be explained using LiDAR techniques. As the Airbone LiDAR techniques have some limitations, bathymetry surveys or SONAR techniques which are used as an alternative of LiDAR technique. SONAR techniques are used to obtain cross sectional river data.

In order to produce a smooth bathymetry in the flow model, many researchers proposed an algorithm for sparse cross sectional river measurement. The river cross sectional data extraction in longitudinal and transverse directions can be done using following three algorithms which are Natural Neighbor (NN), linear interpolation and Inverse Distance Weighting (IDW). In 2D model, the observed and simulated water stages are compared using three algorithms along the original and resampled cross section data. The river stages were simulated using 3D model by obtaining resampled cross sectional river data on the basis of linear interpolation method during high and low flow conditions in the river Tsengwan. The conclusions were drawn after sensitivity analysis of vertical eddy viscosity and drag coefficient under linear interpolation method based on 2D and 3D models.

Tectonic Geomorphology

Tectonic geomorphology describes the relation of tectonic activities and erosional processes with geomorphic features. The tectonics uplift of spatial patterns is related to the platform changes. Gurnis [17] proposed discrete uplift and different stages of landscape give rise to mountain belts. Subsequently, Hager [18] suggested a model for the development of landscape which shows the response of surface topography to a period of relative uplift and sustained waxing. It is stated that the lithospheric strength and erosional procedures limit the growth of surface topography [19].

Tectonic and Climatic Forcing of River Incision

Changes Stream Geomorphology

Dynamic equilibrium will be established in the river system after disturbance. After channelizing or removal of alluvial material the stream will deteriorate its natural state. After deterioration water quality will be reduced while erosion and sediment transportation will be increased. Thus, continual maintenance is required to control the natural state deterioration of stream.

Changes in stream profile are triggered by extracting alluvial materials from the stream bed. When the balance between the supply of sediment and sediment carrying capacity of streams is disturbed by the changes brought to flow regime, the stream bed is eroded and the channels deepen in the stream bed.

At a point in the stream bed, velocities of flow increase because of steeper gradient creating a Knick point. The Knick points will move upstream by a process called head cutting when the increase in flow velocities erode the stream bed. The movement of Knick point continues until the stream gradient stabilizes. Large amount of stream sediments is released, transported and deposited in downstream by head cutting. The form of channel is changed by deposition of stream sediments in deep holes of stream. As the cross-sectional area of channel increases, its flow capacity is also increased which effects the movement of sediments.

The energy dissipation of larger floods across the plain is low as they are restrained in the modified channels. Thus, the stream energy during flood is increased which cause erosion, increases transport and supply of sediments. The stream banks collapse due to deepening of stream bed which increases stream height that led to collapse and erosion. Extensive collapse of river banks widens the streams which increases its flow capacity, transport and supply of sediments downstream.

When the gravel is removed from the stream bed, the materials liable to erosion are exposed by bars of river. This causes excessive scouring and movement of bed sediments which causes removal of materials and loss of stream roughness. Removal of materials including boulders and woody debris may reduce health of ecosystem and structural integrity of stream.

Flood carrying capacity of stream is increased by channelizing, which can result in unintentional erosion downstream and upstream of a channel. The velocities of flow are also increased by increasing the slope. Sudden changes in the slope can cause degradation and erosion of the channel upstream, and aggradation of the channel downstream. The importance of increased flow velocities is dependent upon the river banks, the bed and the condition of the riverine vegetation cover. The materials such as gravel and cobbles provide resistance to erosion and the riverine vegetation also decrease the chances of erosion by decreasing the flow velocities. The increasing flow velocities and flow volumes may destabilize the river banks and can trigger many other changes in profiles of stream. Stream flow affects the surface and ground water and can trigger changes in local hydrology which can cause unintended changes in water flow. The removal of stream gravel and alluvial substance may cause reduction of bank storage, lowering of water table, drainage of associated wetlands, variations in stream flow and uniform stream state.

Channelizing

The flow velocity and capacity can be increased by smoothing and flattening of river banks. The straightening of river banks may have following outcomes:

- Flood flow is increased downstream by increasing flow velocities.
- Greater water flow may cause unintentional changes in stream course.
- Improved drainage of land near stream can cause reduction of water in stream during dry season.

Stocks of soil left on flood plain may trigger changes in hydraulics of stream during flood.

- Modified slope of stream after cut-off
- Natural slope of stream.
- Stream flow
- Downstream sediment deposition
- Sediment extraction
- Bed erosion moves upstream
- Stream flow
- Natural stream channel

The diversion of channel will decrease the length of channel increasing the slope of stream which causes head cut erosion and increased flow velocity.

Damages infrastructure

Excavating of the stream causes erosion which may harm private and public properties. Utility lines and submerged pipelines may be exposed and bridge piers may get eroded by channel incision. Downstream flood aggravation may elevate the risk of destruction of flood protecting structures and infrastructure.

Increased sediments supply and transport downstream by excavating the streams may demean stock and domestic water transportation. Sediment input or runoff from nearby lands may be triggered by a new channel course. Excessive quantity of nutrients, pesticides and salts are discharged into the stream by agricultural lands runoff.

Reduces recreational and aesthetic values

Increased sediments and pollutants that are visible in water may reduce recreational activities including swimming, fishing and bird watching because these activities require pollution free clean water. Landforms and vegetation covers must be preserved to conserve the aesthetic values of stream.

Study area

Swat is a valley and district located in the province of Khyber Pakhtunkhwa. It is known for its outstanding and tremendous beauty. During the visit of Queen Elizabeth, this place was named as the Switzerland of the East. Swat was a Buddhist district and early it was a part of the Gandhara district which is self-grooming district with the total population of 2309570 according to 2017 census. Swat is comprised with cooler and wetter climate condition with the average elevation of about 980m.

Swat lies between the foothills of Hindukush mountain range between 34°-40' to 35° N latitude and 72' to 74°-6' E longitude. Swat has major intentional importance as it is located in the region where central Asia, south Asia, china meets and it is the part of North Frontier province of Pakistan. The altitude of swat valley is 975.36m to 2900m and is located 257 kms to NW of Islamabad territory and 176 kms to NE of Peshawar. In Sawat valley, Falak Sher/Sar peak is the highest peak of Hindu Kush range which is of 5918 meters.

The Swat peak point is in Tirich Mir (7,708 m) in Chitral District. The peak point of swat is located in Tirich Mir at 7,708m in district Chitral. The peak point of swat divides the

Amu Darya valley from north to south from Indus river valley. It runs to Swat buttresses in the East to a point where Pakistan, Afghanistan and China borders meet known as Pamir range. Finally, it merges into western minor ranges of Afghanistan moving through the Southeast part of Pakistan.

The mountain ranges of the Swat reveals a general trend, as it stretch westward, and extend from 4,500 to 6,000 meters (14,700 feet to 19,100 feet), near Kabul (in the middle). These ranges attain the height of 3,500 to 4,000 meters (11,500 feet to 13,000 feet). The average altitude of Swat is 4,500 meters (14,700 feet) which stretches about 966 kms (600 mi) laterally; with its 240 kms (150 mi) median north-south measurement. Swat Mountains covers only 600 kms (370 mi) of entire Swat ranges mapped in Figure 1.

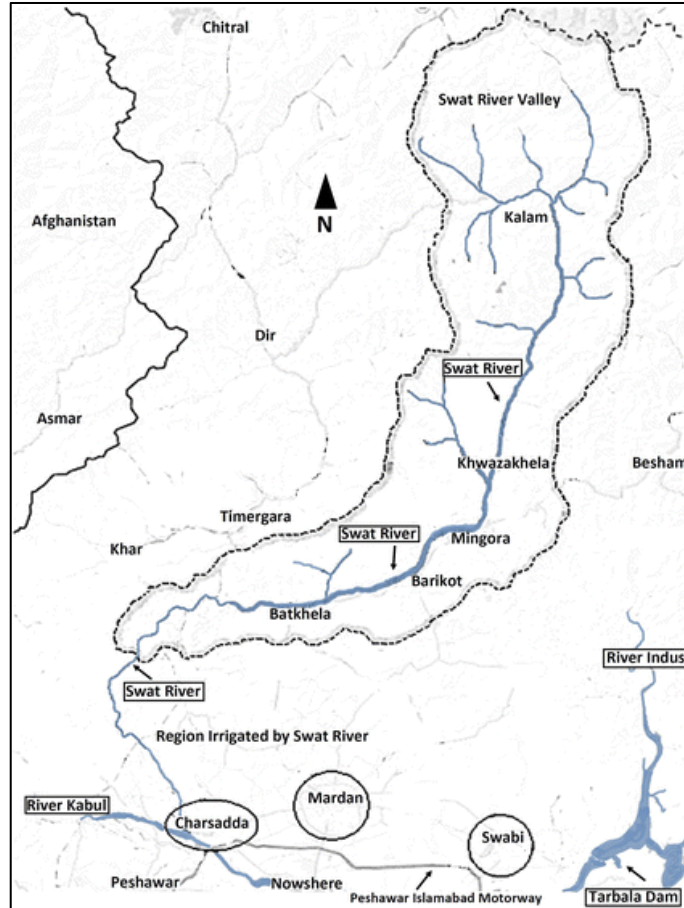


Figure 1. Swat River

Swat Seismology

In context of seismicity, the most active regions of Swat system lies along the boundaries of NW Pakistan, far NE Afghanistan, and Tajikistan. As the activities of subduction of oceanic lithosphere are rare, therefore oceanic lithosphere subducted with seismic activity of compression depth (70-300km). The most dynamic region of compression depth seismicity is associated with the Pamir-Hindukush central Asia Swat region and these dynamic regions are not clearly linked with the progressing subduction of lithosphere. In the past, many seismologists explored the Swat region as mapped in Figure 2.

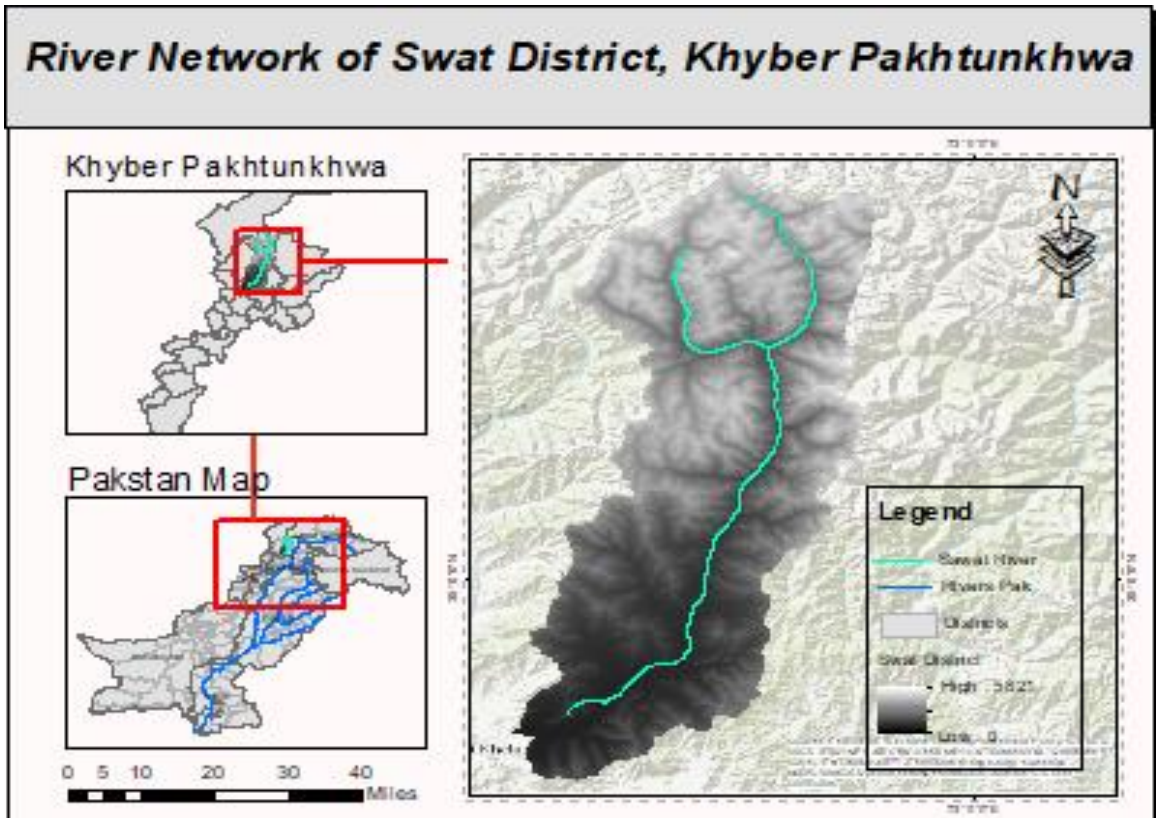


Figure 2: Map of Swat District, Khyber Pakhtunkhwa Province of Pakistan

Swat River

Swat river is known as a Persistent river located in the northern area of province Khyber Pakhtunkhwa. The river starts from the region Swat Kohistan and flows downstream in a narrow ravine up to Baghdheri with convergence of Ushu and Gabral tributaries. The major streams of swat river such as Gabral and Ushu Gols also changes its gradient at many places and this change is not only due to some mountains but due to a high quality Alluvial fans. As these tributaries fed by the glaciers water flow through the Kalam valley with a rushing speed in a narrow valley up to Madyan and lower plain areas of Swat valley up to Chakdara. The ruptures in tectonic plate are mapped in Figure 3.

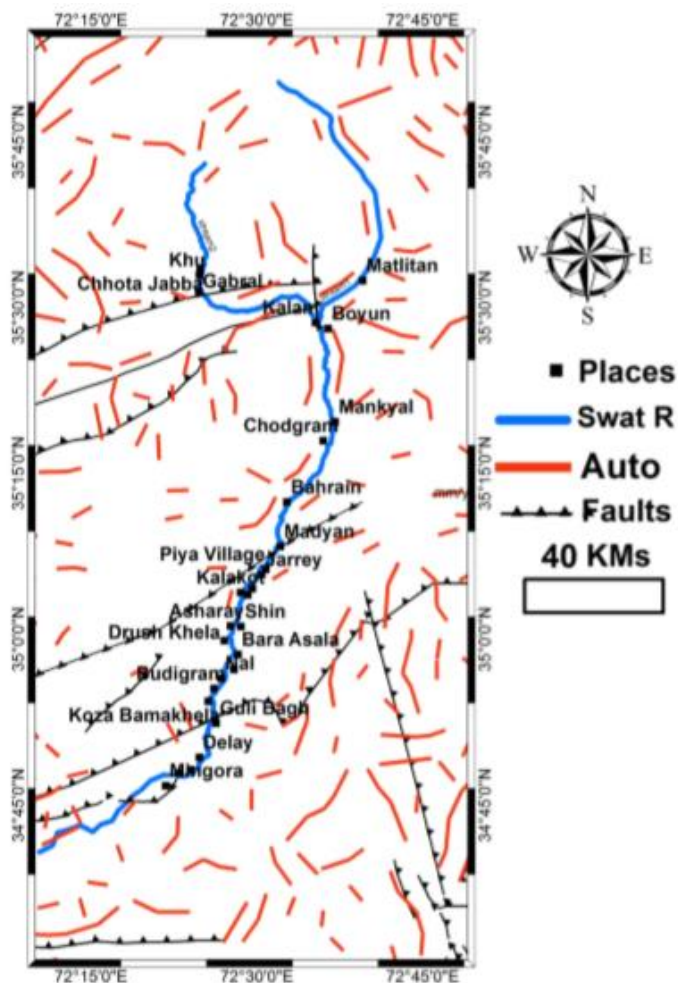


Figure 3. Fault map of study site.

MATERIAL AND METHODS

Neo-tectonic activity in Swat ranges is determined using remote sensing data.

Data Acquisition and Processing:

Essentially two sorts of datasets are utilized to map dynamic surface deformation in Swat. This datasets contains the Sentinel-2 and SRTM Digital Elevation Model data.

Stream definition and Segmentation

Stream segmentation defined the how smaller the stream network allows for the assigning of the same unique value to stream cells situated within the same stream segment.

Watersheds Delineation and Polygon Processing

In watershed delineation model, the grid processor needs following grid layers: sink points, flow accumulation, and flow direction. Basically, it is grid catchment area draining into each stream segment. The watershed delineation helps us to identify the area with minimum and maximum flow. It is done by drawing lines on a map to identify a watershed's boundaries. These lines are drawn using information of contour lines.

Longitudinal Profiles of River:

Geomorphological analysis of river systems should consider landforms associated with river dynamics in complete hydrographic context. It means, the simplest morphological expression that contains the greatest amount of information is the longitudinal profile of the river. The procedure will create a line of flow over a river channel of DEM, generate a profile for the vector set and apply a statistical process to remove topographic errors.

D8 algorithm is used to find flow directions of topographic plan. This method highlights "flow" of each pixel along one of its eight native pixels, it demonstrates that D8 method requires DEM technique to extract stream method without any depression. Flow patterns in planes are analyzed by "Imposed gradients" method. The most supporting is D8 grid as it gives vector data as output. The output vector extracts data from a single or many dislodged basins. Outlet pixel include all pixels for a specific basin. All these basins have a variety of attributes to contribute a particular region. First one encounter attributes for all channels links in the river network while second one is a stream file that encounters attributes for every stream in the river network system. Finally, drainage area grid is created to calculate concavity.

Calculation of Concavity and Steepness

The stream model explains detachment-limited incision which occurs in bed rocks. The calculation depends upon this model. Area drainage and gradient of channel is determined using Power law.

$$dz / dt = U(x,t) - K A^m S^n \quad \text{Eq. 1}$$

In the above equation, dz/dt shows the variations in rate of change of channel's elevation. U represents the rock uplift rate comparative with fixed foot level. The symbol A states upstream area, K is the dimensional coefficient of erosion, S shows the value of gradient of channel at local level and the values of m and n remain positive in contrast with the hydrology of basin and the erosions. If this condition is analyzed as Steady - State (dz / dt = 0), taking U and K uniform and taking m and n as constants, the equation (1) can be resolved into an equilibrium expression.

$$S = (U/K)^{1/n} A^{-(m/n)} \quad \text{Eq. 2}$$

Equation 2 represents the relationship between Power and Law to determine the channel gradient and drainage area for natural landscapes:

$$S = k_s A^{-\theta} \quad \text{Eq. 3}$$

Here the coefficient (U / K)^{1/n} is steepness of channel, the values of k_s and the ratio m/n is the essential channel concavity that is equals to the actual concavity θ by taking uniform K, U, m, and n. Taking Log on both sides of the equation 3 we get:

$$\log s = -\theta \log A + \log k_s \quad \text{Eq. 4}$$

In equation 4, the concavity θ, steepness k_s and the regression is - θ also the intercept is log k_s.

Results and Discussions

The interpolated concavity map is shown in Figure 4.

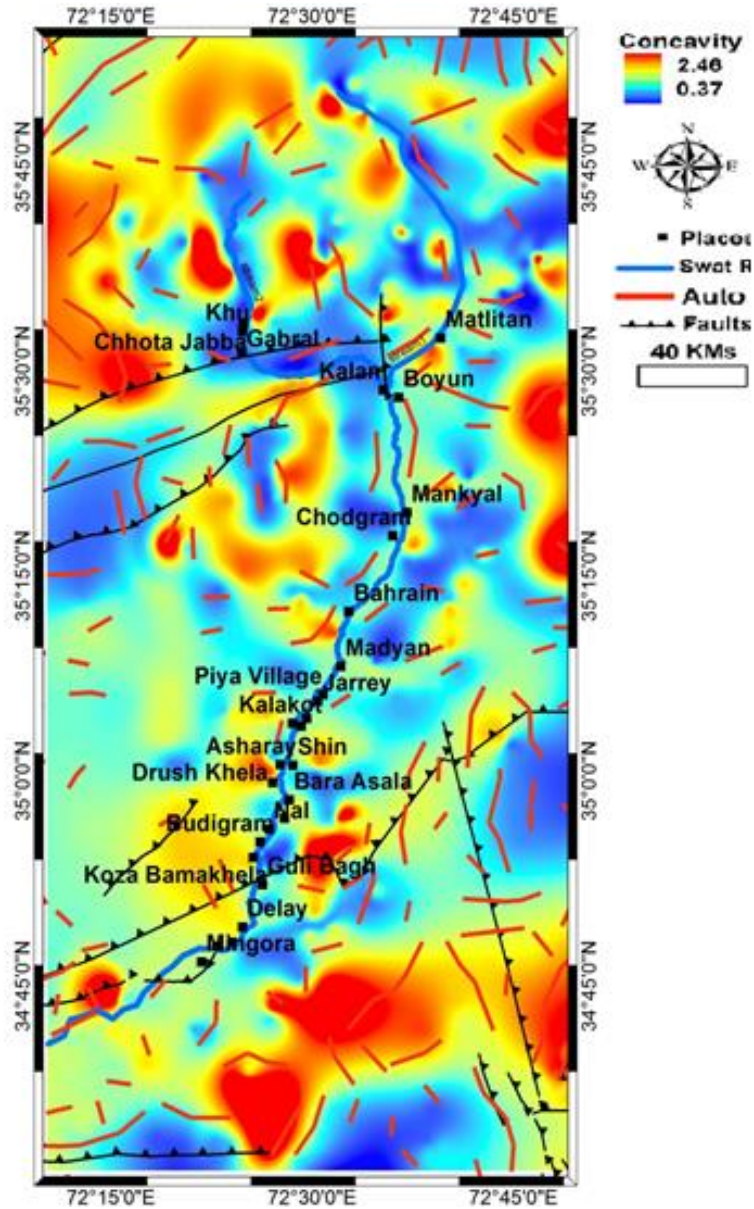


Figure 4. Interpolated concavity map for Swat valley and surroundings. Thick black lines with teeth symbols show published geological faults and red lines show SRTM DEM based automatically extracted faults.

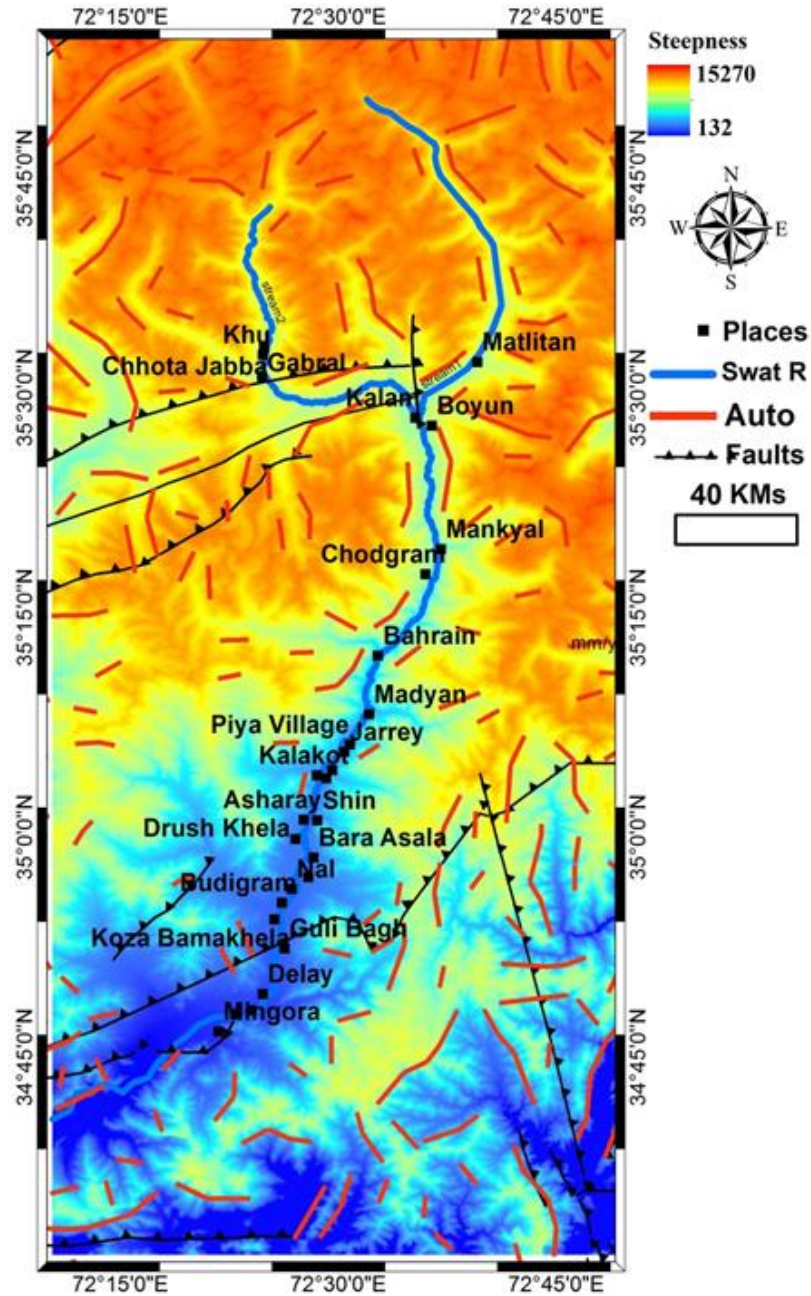


Figure 5. Interpolated steepness map (K_s) for Swat valley and surroundings.

The northern side is highly steep therefore the pressure of water flow is very fast which move sediments and raw material leading to high pressure of erosion and incision. Steepness is less in southern region which is showing gentle slopes therefore this situation leads to less erosion/incision.

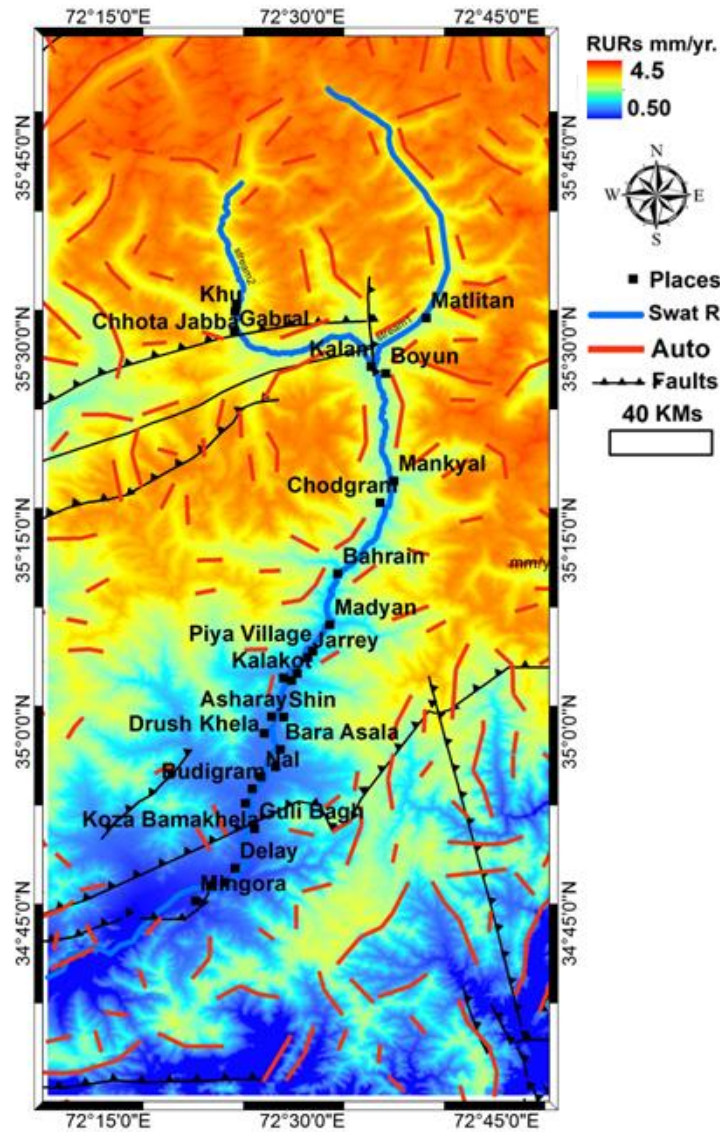


Figure 6. Relative uplifts rates of Swat Basin

Figure 6. Map showing relative uplifts rates of Swat Basin, reddish orange part of the map is dominated by the regional uplift in the context of India Eurasia collision and it is upper swat. While lower swat below Mingora is showing lesser uplift rates but still in the south corner, there is cluster of lineaments along the Main Mantle Thrust (MMT) which is a neotectonics.

Topographic development of Swat valley and the relative uplift is demonstrated using geomorphometric maps and indices. The concavity and steepness of the stream are analyzed using stream profile analysis and incision detachment model which showed 236 large and small streams originated from the region. Steepness and concavity index values were described by regression model to carry slop and stream profile analysis. Non equilibrated profiles specify relative reinforcement of waterway triggering the incision, narrowing, and erode neotectonics components which in turn represent Knick points glided

by stream enforcement forces. The concavity index map shows that, the effect of erosion is more dominating in Gabral valley, Ushu valley, Chhota Jabba, between madayan and Mangora and towards the Shangla Pass along the syntax which is situated south east of Mangora, on the south east of MMT (Main Mantle Thrust). Thus, the low concavity index, high uplifts and disturbed profiles are shown by the streams located in this region which indicate surface smoothness and activeness. Likewise, the upstream of Swat river starting from Madayan till upper swat and NW and NE of Gabral River and Ushu have relatively higher uplift rates. Due to this reason, the local topography has been pushed many kilometers away by the greatest shear zone which is located near NNE of the MMT and northern Dir Thrust. Stream profile analysis was performed for 116 streams. A demonstration of stream 1 is shown in Figure 7.

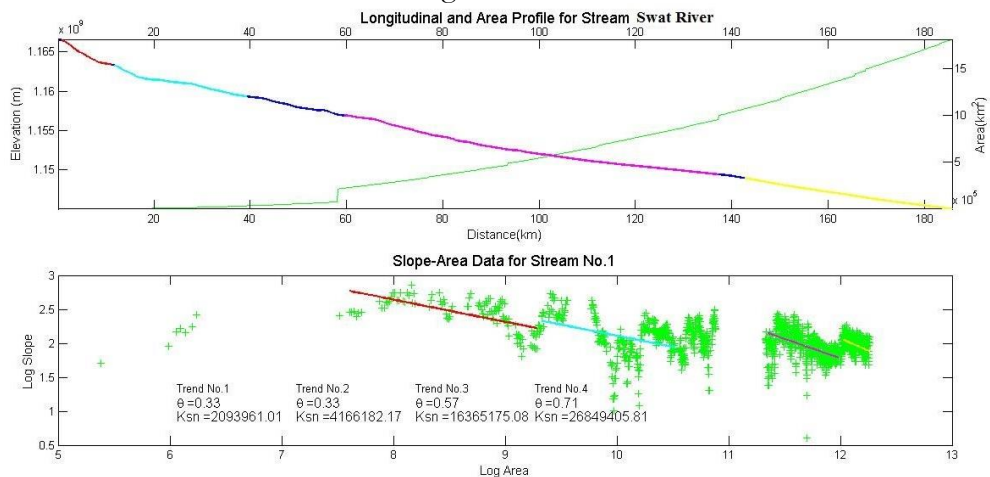


Figure 7. Stream profile analysis.

Conclusions:

The automated drainage network based on DEM is an important tool for computer-based analysis of stream profiles as it gives information about the landscape and surface deformation in the study area. The Soan River exhibits a change in the course of its behavior which is related to the neotectonics and underneath lithologies of the Potwar Plateau. The relative uplift rate map of the study area indicates that Swat Valley is deformed tectonically more (higher uplift) in upper half as compared to the Lower half. The Geomorphometric features are important and effective indicators for neotectonic studies in a young tectonic regime with low elevation. SRTM DEM-based isobase technique has been quite useful, quick and efficient technique for the morphotectonic investigation. Isobase maps permit the quick, delineation, recognition and orientation of neotectonics that present either poor or very less exposed expressions on the thematic maps.

Author's Contribution. All authors contributed equally.

Conflict of interest. Authors declare no conflict of interest for publishing this manuscript in IJIST.

Project details. Nil

REFERENCES

1. Arnold, J.G., Srinivasan, R., Muttiah, R.S., Williams, J.R., Large area hydrologic modeling and assessment. Part I: model development. *J. Am. Water Resour. Assoc.* Vol 34, issue 1, pp:73–89, 1998.

2. Arnold, J.G., Muttiah, R.S., Srinivasan, R., Allen, P.M., Regional estimation of base flow and groundwater recharge in the upper Mississippi River basin. Vol 227, issue 1, pp: 21–40, 2000.
3. Beasley, D.B., Huggins, L.F., Monke, E.J., ANSWERS: a model for watershed planning. Trans. ASAE , Vol 23, issue 4, pp: 938–944, 1980.
4. Chen, J.Y., Adams, B.J., Integration of artificial neural networks with conceptual models in rainfall-runoff modeling. J. Hydrol. Vol 318, pp: 232–249, 2006.
5. Dawson, C.W., Wilby, R.L., Hydrological modelling using artificial neural networks. Prog. Phys. Geog. Vol 25, pp: 80–108, 2001.
6. De Roo, A.P.J., Wesseling, C.G., Ritsema, C.J., LISEM: a single event physically based hydrological and soil erosion model for drainage basins: I. Theory, input and output. Hydrol. Vol 10, pp: 1107–1117, 1996.
7. Bell, T. H. Statistical features of sea-floor topography. Deep Sea Research, Vol 22, pp; 883–892, 1975.
8. Birnir, B., Smith, T. R., & Merchant, G. E. The scaling of fluvial landscapes. Computers & Geosciences, Vol 27, pp: 1189–1216, 2001.
9. Memoir - Geological Society of America, 201, 66. Chase, C. G. Fluvial landsculpting and the fractal dimension of topography. Geomorphology, Vol 5, pp: 39–57, 1992.
10. In P. R. Wilcock & R. M. Iverson (Eds.), Prediction in Geomorphology, Geophys. Mono, Vol. 135, pp. 103–132, 2013.
11. Durand, M., Gleason, C. J., Garambois, P. A., Bjerklie, D., Smith, L. C., Roux, H., et al. An intercomparison of remote sensing river discharge estimation algorithms from measurements of river height, width, and slope. Water Resources Research, Vol 52, pp: 4527–4549, 2016.
12. Fishwick, S. Surface wave tomography: Imaging of the lithosphere-asthenosphere boundary beneath central and southern Africa?, Vol 120, pp: 63–73, 2010.
13. Gallant, J. C., Moore, I. A., Hutchinson, M. F., & Gessler, P. Estimating fractal dimension of profiles: A comparison of methods. Mathematical Geology, Vol 26, issue 4, pp: 455–481, 1994.
14. Giresse, P., Hoang, C.-T., & Kouyoumouzakakis, G. Analysis of vertical movements deduced from a geochronological study of marine Pleistocene deposits, southern coast of Angola. Journal of African Earth Sciences, Vol 2, issue 2, pp: 177–187, 1984.
15. Goren, L., Fox, M., & Willett, S. D. Tectonics from fluvial topography using formal linear inversion: Theory and applications to the Inyo Mountains, California. Journal of Geophysical Research: Earth Surface, Vol 119, pp: 1651–1681, 2014.
16. Guiraud, M., Buta-Neto, A., & Quesne, D. Segmentation and differential post-rift uplift at the Angola margin as recorded by the transform-rifted Benguela and oblique-to-orthogonal-rifted Kwanza basins. Marine and Petroleum Geology, Vol 27, pp: 1040–1068, 2010.
17. Gurnis, M., Mitrovica, J. X., Ritsema, J., & van Heijst, H.-J. Constraining mantle density structure using geological evidence of surface uplift rates: The case of the African superplume. Geochemistry, Geophysics, Geosystems, Vol 1, pp: 1020, 2000.
18. Hager, B. H., & Richards, M. A. Long-wavelength variations in Earth's geoid: physical models and dynamic implications. Philosophical Transactions of the Royal Society London A, Vol 328, pp: 309–327, 1989.

19. Hancock, G. R., Martinez, C., Evans, K. G., & Moliere, D. R. A comparison of SRTM and high-resolution digital elevation models and their use in catchment geomorphology and hydrology: Australian examples, *Earth Surf. Processes Landforms*, Vol 31, pp; 1394–1412, 2006.



Copyright © by authors and 50Sea. This work is licensed under Creative Commons Attribution 4.0 International License.



Generation of Digital Surface Model (DSM) USING UAV/ QUADCOPTER

Huma Ahmed Hassan¹, Syed Amer Mahmood¹, Saira Batool², Areeba Amer⁴, Mareena Khurshid³, Hina Yaqub¹, Sajjad Ali Gill⁵

¹ Department of Space Science University of the Punjab Lahore.

² Centre for Integrated Mountain Research (CIMR) University of the Punjab Lahore.

³ Department of Geography University of the Punjab Lahore.

⁴ College of Earth & Environmental Sciences (CEES) University of the Punjab Lahore.

⁵ Department of Sports Science University of the Punjab Lahore.

* Correspondence: Marina Khurshid and Email : marinakhurshid@gmail.com

Citation | Hassan.H.A, Mahmood.S.A, Batool.S, Amer.A, Khurshid.M, Yaqub.H. Gill.S.A,
" Generation of Digital Surface Model (DSM) USING UAV/ QUADCOPTER"

International Journal of Innovations in Science & Technology, 2020 Vol 2 Issue 3 PP 89-107

Received | Aug 15, 2020; Revised | Sep 11, 2020; Accepted | Sep 13, 2020; Published | Sep 15, 2020.

Abstract

Satellite imageries are being used as primary source of information due to their vast coverage and high temporal resolution. Unmanned Aerial Vehicle (UAV) is being used these days because of its accuracy, autonomous flights, cost effectiveness and rapid overview of data. UAV provides a fully or partially autonomous image acquiring platform which is devoid of any manned flight controller. In this research Phantom 3 advanced Quadcopter was used for an image acquisition plan for generation of Digital Surface Model (DSM). Two designs were drawn through this workflow for the reconstruction of Department of Space Science and technology in university of Punjab. For the first design 3D quadcopter is hovered at the height of 120 feet (37 meters) which covered an area of 83 x 130 meter, frontal and sidewise overlapping is 80%, and the camera is kept at an angle of 70° for the double grid type pattern. For second mission design a circular flight is taken to obtain images at the height of 27meters with coverage area of (107 x 106) meter, 45° camera angle and 10° circular angle. For reconstruction of urban area, quadcopter is hovered at relatively greater height of 210 feet (64 meters), following the double grid pattern. In order to attain desired GST, the camera is flown at a constant height over the Area of Interest (AOI). The highly overlapped images obtained using Phantom 3, advanced Quadcopter are then processed using Pix4d software for processing of images. Initially, the common points of adjacent images are matched automatically. After matching similar points, additional geographic information of coordinates and z-value of elevation associated with it is generated in 3D space by sparse point cloud. Then a detailed 3D model along the precise geo location is obtained using dense point cloud. A study surface area and its texture are generated using

3D mesh. Finally, a desired 3D surface model is accurately generated containing desired AOI. The results are analyzed using UAV imagery to generate high resolution DSM. DSM for construction of urban area of Department of Space Science was generated at a very high resolution of 3.55cm and 1.8cm respectively. The accuracy of geo locations can be improved by using GPS loggers or by taking the GCPs. It is suggested by many authors that 3D surface model of reconstruction of building is quite accurate geographically and geometrically, after the comparison of bundle block adjustments, Ground Sampling Distance (GSD) value, 3D matching and average point cloud density of DSM. Thus, the 3D surface models are used in parameters, features extraction and estimation of values including depth and elevation values, in texturing, 3D data collection for 3D visualizations, 3D roof tops and building facades and contour maps and orthodox photos.

Keywords: DSM, UAV image high resolution, Quadcopter

Introduction

Imaging system based on Ghost 3 Quadcopter used to generate DSM, it is an accurate representation of next generation of DJI quadcopters. Its features include a compass, flight controller, barometric, gyroscopic, vision positioning system, GPS, and RTH sight, and a return system that returns the quadcopter to the position from where the flight was started [1]. The quadcopter is accountable for a precise flight even in the absence of GPS signals because of vision positioning system. It has 4480mAh intelligent flight battery which provides maximum flight for 23 minutes. The aircraft has a weight of 1280 grams which also include propellers and battery [2]. A representation is shown in Figure 1.

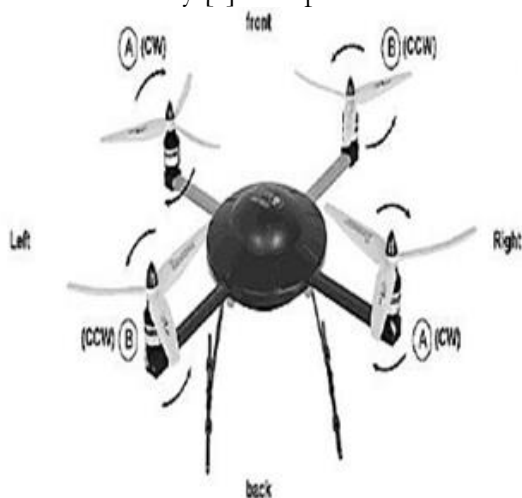


Figure 1: Physical Structure of Quadcopter

Camera and Gimbal

The phantom 3 is advanced technology paired with a mini-CMOS camera sensor. This sensor accurately records videos up to 1080p and take images up to 12 megapixels. In order to minimize distortion while camera is capturing views in air, the $f/2.8$ aperture lens is used with a fixed focal length of 20mm with a field view of 94° . The camera has a 6.17 mm \times 4.55mm (4032 \times 3024 pixels) CCD sensor with image size. The video size 2.7K (2704 \times 1524 pixels), but due to small size of pixel, videos are not recommended. The raw photographs are stored in a class 10 compatible Micro SD card with a maximum capacity of

64GB which display telemetry data of a flight and status of aircraft. Certain other variables are automatically recorded in the aircraft's internal storage [3].

A stable platform is provided by 3axis stabilizing gimbal system to capture constant and clear photographs and videos for a digital coupled camera [4]. Tilt motion ranging from -90° to $+30^{\circ}$ of the digital camera is controlled by gimbal system.

DJI Pilot App

DJI is a mobile application especially designed for Phantom 3 Advanced aircraft, [5]. This application controls gimbal, adjust the camera and field, shares photos and videos. This app is recommended for best practice of aircraft.

Flight

The Phantom 3 Advanced quadcopter can take appropriate images in $<10\text{m/s}$ wind speed as it is sensitive in severe weather condition. Its flight is supported usually in open regions which are devoid of any crowd, obstacles, tall trees, high voltage electricity lines, and metallic objects and GPS sensors in sunshine hour [7]. This system isn't always legitimate close to the polar regions [8].

Flight Planning

A number of deliberations are required for mapping and planning of flight. Flight operation is planned either physically or automatically through GPS waypoints. In order to construct a map of a regular flight pattern, the manual controls prove more effective and valuable in self-directed and real time covering missions. Drone mappers usually operate the drone according to their expertise, some operate autonomously and some mappers operate the drone manually. Pilots should have complete knowledge of driving the drone whether physically or automatically. Drone should not move out of line of sight to pilot unless the pilots have particular requirement, enough practice, and authoritarian permission to move apart from line of sight. Drone may show unpredictable behavior due to bad weather conditions, signal interference, GPS hindrance, and other nominal faults. Drone is preferred to fly manually in lower forest canopies and in populated towns. Before beginning, the mission areas should be inspected and flight barriers should be analyzed. Before takeoff, pilot must have the ground survey of the mapped area [9].

Designing the flight orientation

One of the major elements of drone mapping is the orientation of a flight rout. Generally, the drone mapping orientations are illustrated as transects and are normally designed in a regular array. Drone generates highly precise map in a flight transect grid by taking images with sufficient overlap. A double grid flight plan is required by 3D surface model to attain all sides elevation of constructed structure which are accurately visible in images. In order to get high quality and more efficient map results some mappers suggest hovering of the drone with different patterns of overlapping at different altitudes within the same area. But a lot of data and storage is required by this process to solve the problems of height difference. While some mappers suggest to maintain invariable altitude for variable attributes of ground.

Pilots use software to locate an area to be mapped by the use of polygon and a camera needed for a required height in order to implement a flight plan using grid pattern. The mission plotter after fulfilling all essential requirements calculates GSD, shows the serial transect of waypoints, total pictures, and other useful material. Before launching, the drone operators modify and plan the amount of overlapping, mission elevation, each of shot

distance, and other constraints. All the data of mission planning is stored either in computer or in-flight controller of drone and also implemented in field work [9]. A demonstration of flight control is shown in Figure 2.

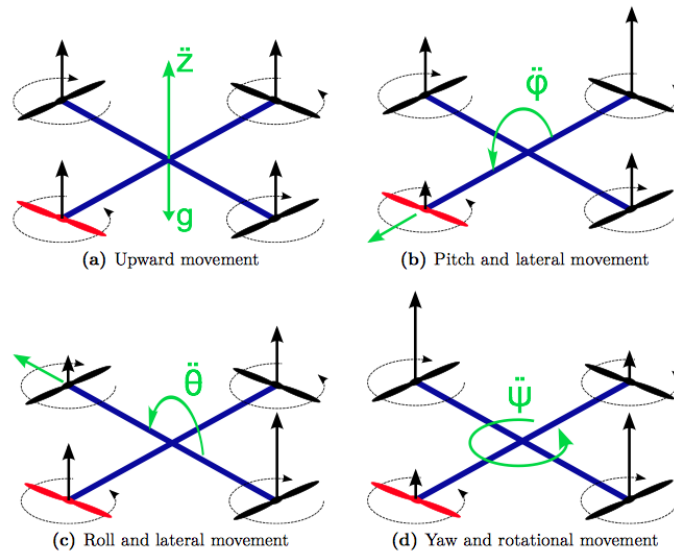


Figure 2: Flight Control of Quadcopter.

Recommended Overlapped Percentage

In order to ensure an adequate amount of sideward and frontward pictorial overlapping, the drone mission mapping is organized and planned. Overlapping values depend upon the situation such as densely populated areas need more overlapping than planned landscapes. According to the tutorial of Pix4D software, 60 percent sidewise and 75 percent onward overlapping is required. The operator needs to adjust the flying speed by adjusting the space present in each capturing photograph, gap between transects, altitude of mission and by the direction of camera in order to achieve a specific degree of overlapping. The recent mission planning software are more affective as they save time by automatically estimating required parameters.

Highly forested zones require higher overlapping. Higher overlapping patterns show that more time and paths for flight are required. Higher overlapping also indicates longer time required for processing, more photographs and increased computer storage for the production of better results [10][11].

Materials and methods

Processing Software

Software selection depends upon the finance, processing power and the task needed to achieve. A variety of softwares are used for drone mapping according to status of drone. Thus, in this research a well-known image processing software the Pix4D is used which has comparatively simple interface and comprehensible guide. It is the most accurate technique to convert aerial images captured by drone or quadcopter technology into 3D digital surface model, 2D rectified mosaics and point clouds. For specialized aerial mapping applications, it offers a creditable track record ranges. The software is upgraded according to the market demands of drone mapping at the regular intervals of time. Moreover, the professional

photography equipment is expensive and has extensive power management requirements. At the time of writing the year 2017, Pix4D priced at 12,500.00 with license and one year lease of \$5,000.00.

1st Project

The area under study is 3D modeling of Space Science Department located in University of Punjab Quaid e Azam Campus Lahore. The Department of Space Science was established in 1985 with $31^{\circ}29'39.7''\text{N } 74^{\circ}17'33.3''\text{E}$ coordinates.

A specific plan of image acquisition is required for the reconstruction of 3D building of study area. In this research, two missions are proposed which have double and circular grid types.

Mission design 1

The circular type mission freely took photographs for the first mission design of Space Science Department (31.494426° , 74.292595°) at 27 meters high covering the area of 107 x 106meter. The drone flies at the camera angle of 45° around the building and 10° circular angle around the building in circular type mission. In order to ensure the desired GSD, the camera need to attain a constant altitude and complete the track of flight over AOI as shown in Figure 3

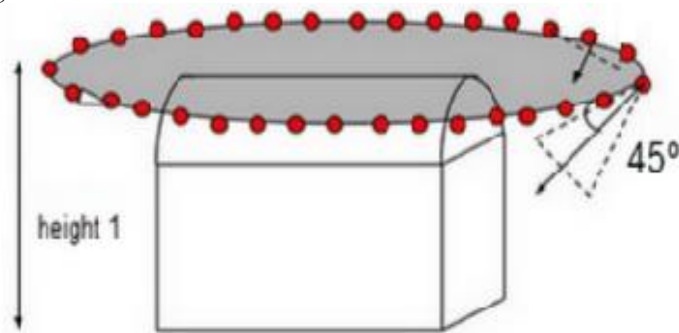


Figure 3: image acquisition plan for circular grid

Mission design 2

In second stage of reconstruction, department of Space Science (31.494270° , 74.2925708°) at 37meters height covering an area of 83 x 130 meter in such a way that all sides of building (north, west, south, east) can be clearly seen on the images taken by double grid pattern. It is recommended that the frontal overlap should be 80 percent with respect to flight orientation and the sidewise overlap between the flying track should be 80 percent with 70° camera angle. The images are recommended to be taken at an angle of 70° and not in the direction of nadir in order to clearly see the sides of building [10] as in Figure 4.

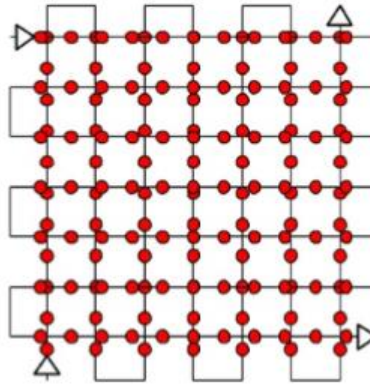


Figure 4: Double grid image acquisition plan
 Table 1 illustrates the specifications of both missions.

Characteristics	Mission Design 1	Mission Design 2
Mission Type	Free Flight Circular	Double grid
Location coordinates [decimal degree]	31.494426, 74.292595	31.494270, 74.292708
Dimensions [meters*meters]	107 * 106	123 * 180
Circular angle [degree]	10	-
Overlap [percentage]	-	80
Camera angle[degree]	45	70
Altitude [m]	27	37

2nd Project

A new policy was designed for the Sui Gas Society in Lahore located at higher altitude for the comparative analysis. The mission design contained double grid type pattern for the reconstruction of 3D urban areas at the altitude of 64 meters in order to clearly see all the sides (north, west, south, east) of buildings in the images. It is recommended that the frontal overlap should be 80 percent with respect to flight orientation and the sidewise overlap between the flying track should be 80 percent with 70° camera angle. The images are recommended to be taken at an angle of 70° and not in the direction of nadir in order to clearly see the sides of building.

a) Computing the GSD for a given Flight Height

The distance between two adjacent pixels is measured from air in order to obtain GSD on the surface of earth. GSD value determines the quality and accuracy of Orth mosaic. This value is inversely proportional to height of flight it decreases as the height increases.

Results and Discussions











Analyzing the Quality Reports

According to the quality report, summaries of both projects are given below in table:
 Table 2: Summary Report of Both Projects

Project	1 st Project	2 nd Project
Name	Space Science Department [Building Reconstruction(DSM)]	Sui Gas Society [Urban Area Reconstruction(DSM)]
Processed	2017-07-26 12:53:23	2017-07-21 11:19:49
Camera Model Name(s)	FC300S_3.6_4000x3000 (RGB)	FC300S_3.6_4000x3000(RGB)
Average Ground Sampling Distance (GSD)	1.79 cm / 0.7 in	3.55 cm / 1.39 in
Area Covered	0.0385 km ² / 3.8486 ha / 0.0149 sq. mi. / 9.5151acres	0.1249 km ² / 12.4944 ha / 0.0483 sq. mi. / 30.8904 acres
Time for Initial Processing (without report)	25m:29s	27m:40s

The name, processing time, camera model and its name, 2D area covered by the project and the average GSD is given in the summary report of this research paper. About 1.60cm GSD is estimated during the first project while the actual average GSD is 1.79cm which are quite close to each other. However, the GSD value in the 2nd project is 3.55cm, the GSD value is increased due to the greater 2D area and increased altitude of 2nd project. Following table describes the quality check report of both projects.

Table 3: Quality Check Report of Both Projects

1st Project		
Images	Median of 39800 keypoints per image.	
Dataset	164 out of 164 images calibrated (100%), all images enabled.	
Camera Optimization	6.7% relative difference between initial and optimized internal camera parameters.	
Matching	Median of 12683.2 matches per calibrated image.	
Georeferencing	Yes, no 3D GCP.	
2nd Project		
Images	Median of 38782 keypoints per image.	
Dataset	186 out of 186 images calibrated (100%), all images enabled.	
Camera Optimization	3.33% relative difference between initial and optimized internal camera parameters.	
Matching	Median of 17736.9 matches per calibrated image.	
Georeferencing	Yes, no 3D GCP.	

The quality check report indicates that all checks are green if the report is good. The yellow check of camera optimization during the 1st project 5-20 percent initial contrast increase, it is tolerated according to the situation while the value is 3.33 percent (<5%) in the 2nd project. The Geo referencing check for both projects is yellow because 3D GCPs are not applied externally. The Phantom 3 Advanced system has automatically georeferenced these projects. All the remaining checks are green. The first column of report shows the keypoint median value on every image, the unique points on the images that are identified are the key points. For a green check greater than 10,000 (>10,000) key points from each image should be extracted, in this research therefore the key points 39800 and 38782 have been taken out for both projects respectively. Second column contains total images which are operated in model rebuilding. It also signifies user restricted images. The check shows green when 95 percent or greater images are rectified in one block. The fourth column identifies the medium of matches per calibrated image which is green for more than 1000 (>1'000) matches.

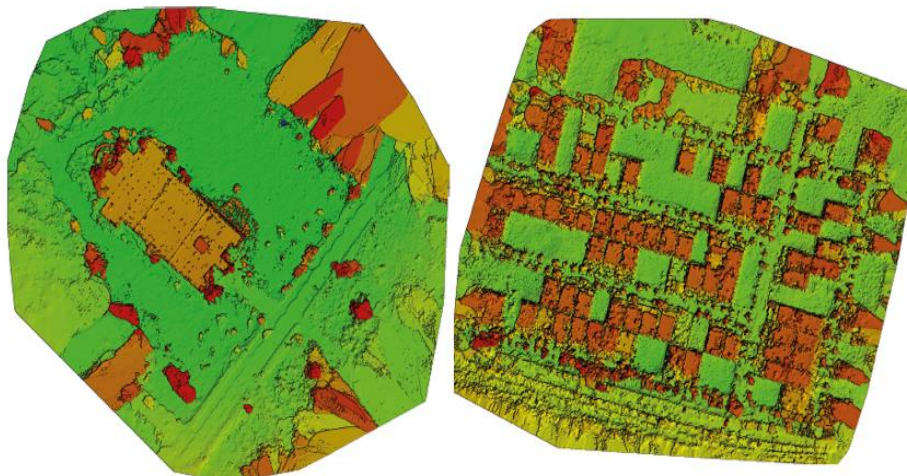


Figure 5: DSM of Space Science Department (Left) and Sui Gas Society (Right)

Calibration Details

Table 4: Calibration Details of Both Projects

	1st Project	2nd Project
Number of Calibrated Images	164 out of 164	186 out of 186
Number of Geolocated Images	164 out of 164	186 out of 186

For both projects from the total number of photographs taken during flight are all gauged and enabled for reconstruction model. These photographs are geologically located.

Original Image Points

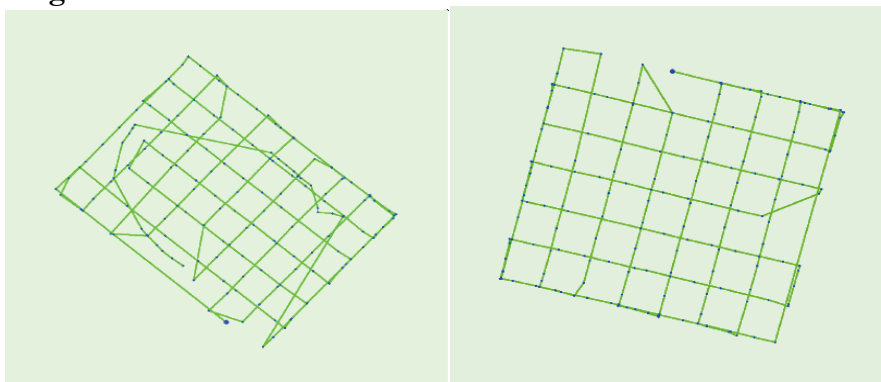


Figure 6: Original Image Points of Space Science Department (Left) and Sui Gas Society (Right)

The geological locations of images corresponding to flight are verified by these figures. According to these figures, first project contains circular and double grid mission design while second group comprised of double grid mission.

Initial and Calculated GCPs/Tie Points Positions

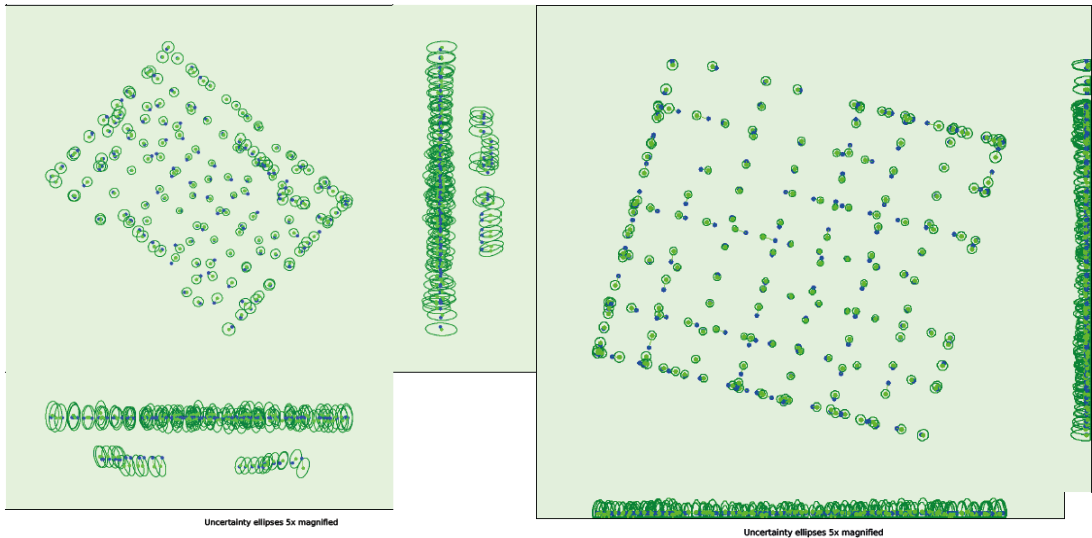


Figure 7: Initial and calculated GCPs/Tie Points Positions of Space Science Department (Left) and Sui Gas Society (Right)

The correlation between initial point (blue crosses) between its calculated region (green crosses) in GCPs is calculated at the top of view (XY plane), front-view (XZ plane), and side-view (YZ plane). Dark green light indicates uncertainty as a result of bricks. If you only use landscape photographs, the size of ellipse is same. The resulting image structure is well centered and well angled, while original definition becomes well known.

Table 5: Absolute Camera Points and Orientation Uncertainties

	X [m]	Y [m]	Z [m]	Omega [degree]	Phi [degree]	Kappa [degree]
1st Project						
Mean	0.556	0.562	1.205	1.073	1.010	0.580
Sigma	0.091	0.096	0.230	0.125	0.145	0.327
2nd Project						
Mean	0.479	0.479	1.161	0.653	0.652	0.352
Sigma	0.073	0.073	0.240	0.014	0.023	0.024

2D Key points Matches

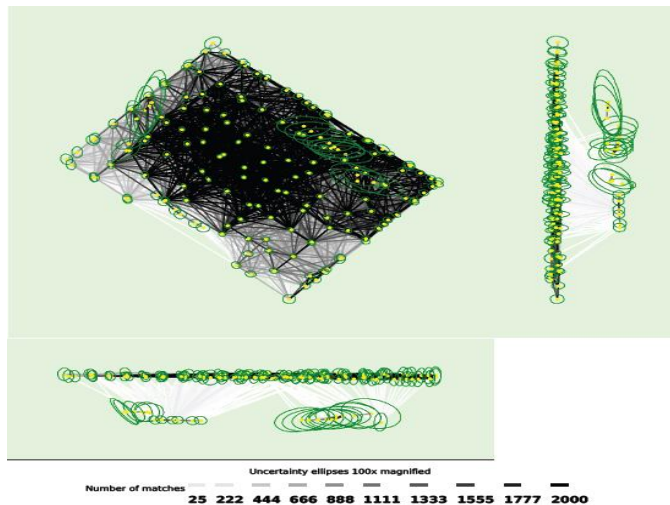


Figure 8: 2D Key points Matches of Space Science Department (Top) and Sui Gas Society (Bottom)

The strong association of 2D key points with manual tie points or other images is shown by darker part while the brighter part indicates weak association. The upper figures are more associated than the lower figures and indicated by dark part. Compared to the first image of the first action there is a lot of relevance between the images shown by the darker part than the bottom of second action image. If sufficient connection is shown between the image and the table, there is only one block. If there are several bricks, the color of each block will be different. In a small image, all the small ellipses of uncertainty are of the same size in the program. Depending on the project, 3D points will be awarded in the corresponding table using the 2D key.

Table 6: 2D Key points.

	1 st Project		2 nd Project	
	Number of 2D Keypoints per Image	Number of Matched 2D Keypoints per Image	Number of 2D Keypoints per Image	Number of Matched 2D Keypoints per Image
Median	39800	12683	38782	177337
Min	27070	360	23205	2848
Max	61671	29080	42778	29250
Mean	39625	13133	38683	18282

Geolocation Details

Absolute Geolocation Variance

The calibrated and geolocated images having imprecise input coordinates, are inaccurate images. Optimized locations of these images are tracked by Pix4D mapper software but the given geolocation table do not highlight and mention these values.

Table 7: Absolute Geolocation Variance

Min Error [m]	Max Error [m]	Geolocation Error X [%]		Geolocation Error Y [%]		Geolocation Error Z [%]	
		1 st Project	2 nd Project	1 st Project	2 nd Project	1 st Project	2 nd Project
-	-15.00	0.00	0.00	0.00	0.00	0.00	0.00
-15.00	-12.00	0.00	0.00	0.00	0.00	0.00	0.00
-12.00	-9.00	0.00	0.00	0.00	0.00	0.00	0.00
-9.00	-6.00	0.00	0.54	0.00	0.54	0.00	0.00
-6.00	-3.00	0.00	6.99	0.61	4.30	0.00	0.00
-3.00	0.00	51.83	48.92	53.05	49.46	48.78	60.75
0.00	3.00	48.17	34.95	46.34	36.02	46.95	39.25
3.00	6.00	0.00	6.99	0.00	9.14	4.27	0.00
6.00	9.00	0.00	1.61	0.00	0.54	0.00	0.00
9.00	12.00	0.00	0.00	0.00	0.00	0.00	0.00
12.00	15.00	0.00	0.00	0.00	0.00	0.00	0.00
15.00	-	0.00	0.00	0.00	0.00	0.00	0.00
Mean [m]		-0.000001	0.00000	-0.000001	0.0000	-0.000007	0.00000
Sigma [m]		1.244621	2.113926	1.259731	2.134670	1.533275	0.411121
RMS Error [m]		1.244621	2.113926	1.259731	2.134670	1.533275	0.411121

The earliest two columns display the minimum to maximum errors ranging from -1.5 to 1.5 which show the geolocation error. These errors indicate accuracy towards X, Y, Z plane, the next three columns show percentage of images indicating geologically located error in X, Y and Z orientation which is basically the difference between calculated and initial geolocations. The precise direction of first project is not related to the errors in geolocations. Geolocation errors in orientation of X and Y of 2nd project and Z orientation of first projected is illustrated in the give table.

Point Cloud Densification details

Table 8: Processing Options of Point Cloud Densification

Image Scale	Multiscale, 1/2 (Half image size, Default)
Point Density	Optimal
Minimum Number of Matches	3
3D Textured Mesh Generation	Yes
3D Textured Mesh Settings:	Resolution: Medium Resolution (default) Color Balancing: no
Advanced: 3D Textured Mesh Settings	Sample Density Divider: 1
Advanced: Matching Window Size	7x7 pixels
Advanced: Image Groups	group1
Advanced: Use Processing Area	Yes
Advanced: Use Annotations	Yes
Advanced: Limit Camera Depth Automatically	No
Time for Point Cloud Densification	05m:05s for 1 st Project 07m:15s for 2 nd Project
Time for 3D Textured Mesh Generation	03m:38s for 1 st Project 06m:11s for 2 nd Project

Multiscale image is used in the point cloud classification in which default image size and densified point cloud density is considered optimal. Minimum number of reprojections is considered the minimum number of matches per 3D point on images ranging from 2-6. For this project the minimum value of effective reprojections is 3, 3D textured mesh is generated using by default resolution medium but balancing algorithm is not considered for this generation. Sample density divider having option 1 is used in advanced 3D textured mesh. In order to match the dense points in the photographs, matching window size and 7x7 pixels size is generally used. One unified point cloud is generated per group of images for making image groups. Point Cloud and Mesh also take into account the used processing area. Camera depth automatically limit the in-point cloud densification. The last columns display time spent on unified point cloud and 3D textured mesh generation for both projects.

Table 9: Results of Point Cloud Densification

	1 st Project	2 nd Project
Number of Generated Tiles	1	1
Number of 3D Densified Points	9686547	11248360
Average Density (per m ³)	514.13	75.62

Point cloud densification show obtained 3D densified points, the number of tiles produced, and the average 3D unified points per cubic meter for the project. Results show that the average density is greater for DSM generation and process a greater number of 3D unified points in the 1st project.

DSM, Orth mosaic and Index Details

Table 10: Processing Options of DSM, Orthomosaics and Index Details

DSM and Orthomosaic Resolution	1 x GSD (1.8 [cm/pixel]) for 1 st Project 1 x GSD (3.55 [cm/pixel]) for 2 nd Project
DSM Filters	Noise Filtering: yes Surface Smoothing: yes, Type: Sharp
Raster DSM	Generated: yes Method: Inverse Distance Weighting Merge Tiles: yes
Orthomosaic	Generated: yes Merge Tiles: yes GeoTIFF Without Transparency: no Google Maps Tiles and KML: no
Time for DSM Generation	02m:24s for 1st Project 02m:45s for 2nd Project
Time for Orthomosaic Generation	07m:25s for 1st Project 07m:20s for 2nd Project

Reconstruction resolution building of Space Science Department is 1.8 [cm/pixels] that is close enough to the calculated GSD value of 1.6 [cm/pixel] and reconstruction resolution of Sui Gas Society urban area is 3.55[cm/pixels]. DSM of urban area reconstruction and Orth mosaic value is given below as a DSM hub, the surface smoothing and noise filters are activated along the sharp smoothing surface. By the use of the inverse distance weighting method, raster DSM is generated and DSM tiles are merged into one file to generate Orth mosaic. Google Maps Tiles, GeoTIFF without Transparency, and KML are not generated in this project. In the last two columns, time is displayed, time spent on both projects for DSM and Orth mosaic Generation.

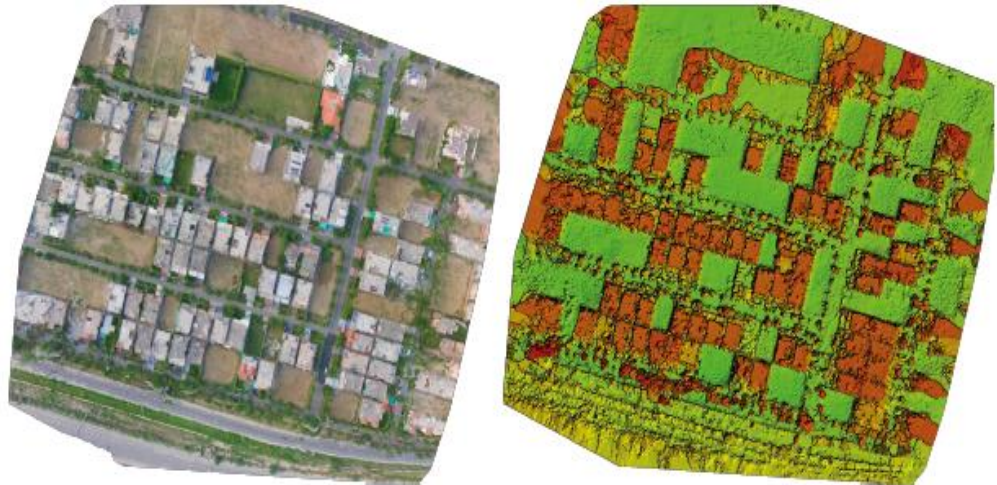


Figure 9: Orth mosaic and the corresponding DSM

Cross-section measurements

For fixed DSM sections, it can be concluded that each feature below the section is defined by a particular resolution due to monitoring. The section line description also shows a white wall with the exact location and elevation, GCP can be used to improve the accuracy of geo referencing and geolocation.

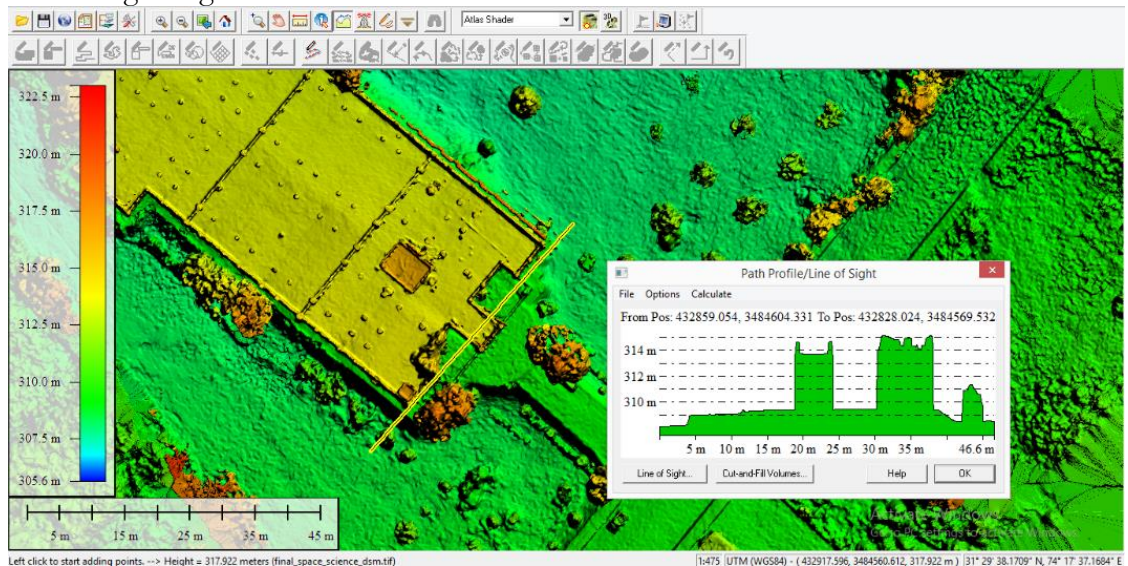


Figure 10. A representation of software

Use of 3D Model and DSM

Modeling buildings and tree heights

The height values of features on the surface of earth can be characterized by the DSM. The value of surface features is calculated by the distance between the ground level connecting the uppermost points. 2D article is removed by extending the 3D model to the certain height. Different parameters such as height and length, circumference, perimeter and building area measurement under reconstruction can be calculated by using DSM.



Figure 11: Volume Calculations for 3D Building Model

Trees

Trees are large 3D species in forestry sector. The height of the tree is determined by the value of building and its relative value. By Extraction of the 3D wooden texture, the vertical side, and the width of each tree is measured. The following figure shows the vertical and horizontal dimensions of tree and tree size.



Figure 12: Volume Calculations for 3D Tree.

Representing 3D Buildings and Extracting 3D Roof Tops

Previously, the construction of 3D building structures were considered expensive and outside the practical abilities. Detailed 3D information is available by survey of urban areas through high-resolution photogrammetry. The model of building truly displays the geometry of building’s roof. 3D buildings and 3D roofs are displayed in figures given below.



Figure 13: Roof Representations for 3D Building Model

Texturing

Texturing represents a geometry outlook of reconstruction of a building contains a building sides and rooftop. Tilted and locally street-level images compose the roof geometry. Thus, in texture maps the images are finally repaired, repeated and revised. These textures display a general building style and don’t exactly match to genuine building. This building generation method used to alter the building style and height, and can be utilized in urban planning.



Figure 14 : Texture Representations of Building and Urban Area Reconstructions

Discussions

3D textured model of building of Department of Space Science and Sui northern Gas Society are analyzed geographically and geometrically for building and urban area reconstruction. RMS is the end result produced by bundle adjustment and its value is less than 1 pixel. Reconstruction of urban area and building area by UAV imagery provide a footprint of approximately 1.8 and 3.55cm, both models can be seen with high quality. But 1st model of building reconstruction of Space Science Department has more high resolution than the 2nd model of reconstruction of urban area due to multiple mission design types and low altitude flight. Better image quality is provided by low altitude imagery. Typically, its density (per m³) is also more than the 2nd mission design due to more amount of 3D densified points. GCPs can prove useful in improving accuracy of model's geolocation for better geo-referencing.

Conclusions

This research shows the design of a UAV designed specifically as databased platform. DSM generation and pre and post processing of UAV imagery is also described in the work plan for flight design. The Phantom 3 Advanced Quadcopter is used to divulge the specifications and flight planning for 3D mapping. In order to obtain uniform and consistence results, required altitude, the direction of flight and patterns of overlapping, GPS sensors and geo referencing methods were applied. The final results of this research display 3D model geographically and geometrically and DSM generation using Phantom 3 Advanced quadcopter imagery for reconstruction of building of Space Science Department and urban area reconstruction of Sui Gas Society at very high resolution of 1.8cm and 3.55cm respectively. Accuracy of geolocation can be improved by taking GCPs. A more high-resolution surface model of Space Science Department is obtained because of its low altitude and mission design type required for the acquisition of data through UAV technology. The results of this research shows that 3D roof top of a building and all facades depth and volume calculations and its texture are completely covered by High resolution DSMs and 3D models. UAV technology is cost effective and autonomous and has high potential for the high-resolution DSM generation

References

1. D R, Sowmya & Deepa, P. & K., Venugopal, Remote Sensing Satellite Image Processing Techniques for Image Classification: A Comprehensive Survey. International Journal of Computer Applications, 2017, Vol 161, issue 11, pp: 24-37.
2. Kuenzer, C. and S. Dech: Thermal Infrared Remote Sensing – Sensors, Methods, Applications. Remote Sensing and Digital Image Processing Series, 2013, Vol 17, pp: 572
3. Baumann, p. P. *History of remote sensing, satellite imagery, part ii*. Retrieved from geo/sat 2, history of remote sensing, (2009)
4. Hassani, Hamid & Mansouri, Anass & Ali, Ahaitouf. Mechanical Modeling, Control and Simulation of a Quadrotor UAV, 2021, pp: 441-449.
5. Harder, C. B. Creating Mirror Worlds; Enabling a new dimension with 3D imagery. In C. B. Harder, *The ArcGIS Imagery Book*. Redlands, California: Esri Press, 2016.

6. Ajayi, Oluibukun & Salubi, Akporode & Angbas, Alu & Odigure, Mukwedeh.. Generation of accurate digital elevation models from UAV acquired low percentage overlapping images. *International Journal of Remote Sensing*. 2017, Vol 38, issue 8, pp: 1-22.
7. Lee, Hou-Hsien & Lee, Chang-Jung & Lo, Chih-Ping, Unmanned aerial vehicle and method for controlling the unmanned aerial vehicle, 2013.
8. de Roos, Shannon & Turner, Darren & Lucieer, Arko & Bowman, David. Using Digital Surface Models from UAS Imagery of Fire Damaged Sphagnum Peatlands for Monitoring and Hydrological Restoration. *Drones*. 2018, Vol 2, issue 4, Pp:45.
9. Greenwood, f. *Drones and aerial observation: new technologies for property rights, human rights, and global development a primer*. New america: valerie altounian, 2015
10. Lillesand, T. M. *REMOTE SENSING AND IMAGE INTERPRET ATION*. United States of America: John Wiley & Sons, 2004
11. Leishman, J.G. *Principles of Helicopter Aerodynamics*. New Yorl, NY: Cambridge University Press, (2000).



Copyright © by authors and 50Sea. This work is licensed under Creative Commons Attribution 4.0 International License.



EVALUATING FOCAL MECHANISM OF SEPTEMBER 24, 2013 AWARAN EARTHQUAKE WITH GEOSPATIAL TECHNIQUES

Israr Ahmad¹, Rana Waqar Aslam^{1,5*}, Lin Li², Muhammad Burhan Khalid³, Waqas Abbas³, Aqsa Aziz⁴, Muhammad Nassar Ahmad¹, Ali Imam Mirza⁵

¹State Key Laboratory of Information Engineering in Surveying, Mapping and Remote Sensing (LIESMARS), Wuhan University, Wuhan 430079, China.

²School of Resource and Environmental Science, Wuhan University, Wuhan 430079, China.

³Punjab University College of Information & Technology, University of the Punjab, Lahore.

⁴Department of Geography, University of Punjab, Lahore.

⁵Department of Geography, Government College University, Lahore.

*Corresponding Author's **Rana Waqar Aslam** Email: ranawaqaraslam@whu.edu.cn.

Citation | Ahmad. I, Waqar. A, et al., "EVALUATING FOCAL MECHANISM OF SEPTEMBER 24, 2013 AWARAN EARTHQUAKE WITH GEOSPATIAL TECHNIQUES". International Journal of Innovations in Science & Technology, Vol 02 Issue 03: pp 108-125, 2020.

Received | Aug 20, 2020; Revised | Sep 15, 2020; Accepted | Sep 18, 2020; Published | Sep 20, 2020

Abstract.

Seismic records from IRIS (NIL, KBL, MSEY, KMI, QIZ, DGAR) were used to compute AWARAN September 24 2013 Earthquake's focal mechanism. Earthquakes are one of the most drastic threats that are likely to cause heavy human casualties and can destroy entire cities within minutes. We processed the waveform data from 6 separate stations for the computation of displacement. The issues related to attenuation have been overcome by the use of low frequencies (0.05-0.1). The crustal model that determines the tensor PREM model's time is determined by minimizing the variance but produces a robust focal mechanism. Inverting the displacement data is applied to recover the moment tensor from the source, calculated the green function with the reversal. GIS-based vectors offault lines were abstracted by the digitization of regional tectonic lineaments and structural maps. We developed synthetic and observed surface shapes with a 100 percent dc correlation. Our understanding of the features of crustal deformation and regional tectonics in the area will benefit from the resulting focus mechanisms. The measured earthquake focal mechanism is similar to a USGS agency hit, dip, and rake.

Keywords: Awaran earthquake, Focal Mechanism, PREM Model, Green Function, GIS.

INTRODUCTION

Seismic tremor or earthquakes are natural hazards which devastate the natural beauty and

ecological balance of a region badly, [1]. The earthquake in AWARAN on September 24, 2013, was triggered by an oblique landslide movement in one of Chaman 's southern strands, [2]. The event took place within the large area of the plate limit established by the MakranCumulative Prism and the Chaman Fault System, [3]. It was situated in a region with well-

defined fault morphologies, [4][5]. but large ($>M7$) historical earthquakes were not previously observed, [6][7]. The surface crust depth (15 to 20 km), the northern slip movement and the internal depth was approx. 80 km as shown [8]. In 1935, the M_w 7.5 earthquake occurred at the Ghzaband fault, [9]. The core mechanisms of medium-depth earthquakes have been clarified mainly in response to the decreasing extension in many subduction areas worldwide, [10]. Seismic procedures provide the highest accuracy of the earth's internal structure than any geophysical method, [11]. This is because elastic waves of any geophysical wave have the shortest wavelength and because the physics which regulates their spatial and temporal sensitivity determines the origin of energy, [12][13].

Several methods for evaluation of point-source and source-time (STF) process for events were established simultaneously, [14]. The use of waveform modelling for calculating focus mechanisms depends on modern tools [15][16][17]. The tensors depend on the spring strength and fault path [18]. The pivoting function or the solving of problems of the plane also implies "beach balls." It gives us a feeling about seismic waves that originate from a complex rupture, involving space and time displacements that are abnormal [19]. Furthermore, it is a plus point to write that is any orthogonal coordinate system since vector and tensor equations are valid irrespective of the coordinates of system. Ordinary data reversal techniques [20] surface waves [21][22][23] and body waves [24][25] have been evaluated and the reversal of broadband seismic charts has been proposed for regional earthquakes [26]. Other methods are also used to evaluate influential movement records and the depth of the source [27].

The ISOLA Interface is used for instance, which carry out certain tasks to access all investment procedures, [28][29]. The green function is measured by wave frequency method, [31][32]. The code is written in Fortran, but the user can control its use through ISOLA-GUI, [33]. ISOLA-GUI creates all the required files with the inspection diagrams (Descartes and Geographies coordinates) for calculating the Green-Inversion function, [34][35]. The relationship representing the percentage of a double pair solution is defined, since it can show problem output in investment. The modules run concurrently and most of them "know" the answer from the user or try to suggest acceptable processing parameters. Significant information on regional and local tectonics is given for medium sized earthquakes in the country, [36]. The focusing mechanisms calculated using only the first direction of movement can thus have a significant effect on the parameters of the coordinating mechanism calculated by these incorrect measurements of the first movement. Depending upon the distribution and consistency of the first motion data, more than one focus mechanism fits to the data. The key benefit of the instantaneous tensor is that seismographs can be reversed to identify the source parameters. Instant tensors for reflection are defined as the movement of an error during an earthquake consisting of nine pairs or nine sets of two vectors.

Material and Methods.

Investigation site.

There were many earthquakes, mostly occurred in coastal areas in Balochistan. District of Awaran is situated (Fig. 1) in the south of the province of Baluchistan (Lat: 27,016 ° N; 65,547 ° E). The red zone for earthquakes in Pakistan is known to be the Mekran range due to tectonic activities. In the remote and inaccessible regions, the earthquake caused widespread destruction and the death toll reached over 825 . Awaran, Ritaj, Jashkur, Nok Jo, Parwar, Dandar and Hoshab were the affected areas. Almost 33,000 homes and 300,000 individuals suffered from the earthquake, [37]. .

The Awaran earthquake was caused by the southern strands of the Hoshab fault in the Chaman fault system. An analysis of high-resolution World View 2 satellite images also confirms the rupture on the left side of the surface. Another confirmation was made of Landsat-8 image for the rupture that corresponded to the Hoshab failure.

The event ruptured the Makran subduction megathrust. The earthquake was 7.7 as measured on the Richter scale. A new island formed called “mud volcano” on the sea floor following the earthquake. The epicenter was situated in an area influenced by the above two crash logics. A complex collection of mountains folding and fissured along the coast and northbound to the west from India and Eurasia's convergence area resulted from relative closeness between the two species [38].

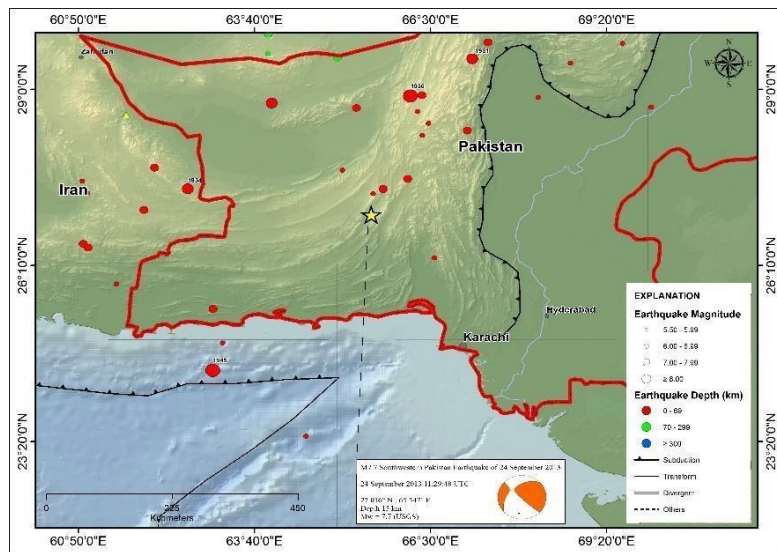


Figure 1. Location of Awaran earthquake September 24th, 2013Awaran

Earthquake in Terms of Richter Scale

Charles F. Richter developed the Richter Scale in 1935. Originally, the earthquake was 7.4MW and then upgraded to 7.8 but later changed to 7.7, on the Richter scale. A heavy shaking (VII) occurred in the nearby town of Awaran on the 24th September, with a major shaking in the big town of Kharan and a heavy shaking in Hyderabad and mild shaking in Karachi.

Table 1. Details of September 24 earthquake

Moment	Magnitude	Depth	Percent of DC	Half Duration	Catalog	Data Source	Contributor
4.418e+20 N-m	7.7 Mww	23.0 km	96 %	-	US	US ³	US ³

Nodal Planes

Table 2. Nodal Planes of the Study Area

Plane	Strike	Dip	Rake
NP1	228°	46°	6°
NP2	134°	86°	136°

Principal Axes

Table 3. The Details of Principal Axes of the Area

Axis	Value	Plunge	Azimuth
T	4.458e+20 N-m	33°	81°
N	-0.080e+20 N-m	45°	309°
P	-4.377e+20 N-m	26°	189°

Tectonics of the Area

Makran tectonic map is shown in the figure 2.

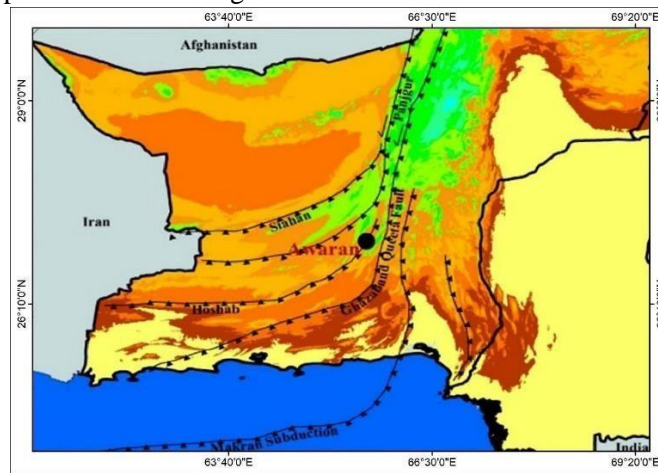


Figure 2. There are major faults on the tectonic map of southern Pakistan. A full black circle is the core location of the Awaran earthquake [18]

It spreads over 400 km north and a 1000 km east, and can subducts under the Euroasian platform by 3 cm / year north of the Arab plate and Ormara.. In 1945, an 8.0 MW earthquake broke the enormous Makran thrust. The Chaman fault system is a 1200 km left-hand failure system adjusted for 3 cm / yr north of India in relation to Eurasia. The Chaman fault system consists of the Ornach Nal, Ghazaband and Chaman 's sinister failures. In the south, the Chaman defects refer to the Seyhan, Punjur and Hushab Makran chains'

defections and those defections are internalised; the tale from India and Eurasia and the shorter one from the Arab Peninsula and Eurasia. The faults left in the side blow sliding faults of the Chaman and Urnash-Nal power the Indians and Eurasians' crash. Landslide systems predominantly form the Makran subduction zone boundaries. The fault system Ornach-Nal marks the eastern frontier, while the fault system Minab-Zendan represents the western border. As the Arabian plate is compressed, in the Makran area and the Chagai Arc, there is a directional tendency between east and west. It implants with an implantation angle of 2-8 degrees at a speed of 19.5 mm per year.



Figure 3. 2013 Earthquake in MW 7.7 Awaran. (a) An aerial view of the Oran area's destruction. (b) A view of the island following an earthquake in Awaran [8]

In Ziarat, the 1.300 Kilometers long Hass Soliman fracture, the Chaman fault and the Sibi basin are regulated by the tectonic and structural patterns. Quetta's local defect structures are comprised of Chaman 's Fault, Chengin Gulat structure, Harnai Tarta Structure, Gzband Gob Chassis, and Mach Chassis. The Makran Coast Fault is 225 km longin south of Ormara and Pasni. The earthquake occurred in the depth of the ground crust over the Makran subduction zone as a result of oblique displacement.

The study is based on the seismic waveforms data which is available at <https://ds.iris.edu/ds/nodes/dmc/data/types/waveform-data/> that was recorded at different stations of the world in response to the earthquake that struck just near the district Awaran on September 24, 2013.

Table 4. Stations Information of September 24, 2013, AWARAN earthquake

Station name	Latitude	Longitude
NIL	33.65	73.269
KBL	34.541	69.043
DGAR	-7.412	72.452
MSEY	-4.674	55.479
QIZ	19.029	109.844

For proper coverage of Awaran earthquake, we set the distance from 0 to 180 degrees using powered. The coverage to the event was ensured from all sides for a better display of results. The start and end time are adjusted such that complete waveforms are obtained. A total 6 IRIS stations for Awaran earthquake were selected such that a proper coverage to the earthquake epicenter was ensured. Our goal was to measure the tensor moment. The first-order seismic tensor is an extensive representation of earthquake sources resulting in a straightforward linear relation with a sequence of green and fundamental error reactions. . So, we choose the station for which waveform data was available for all N, E, Z and time components.

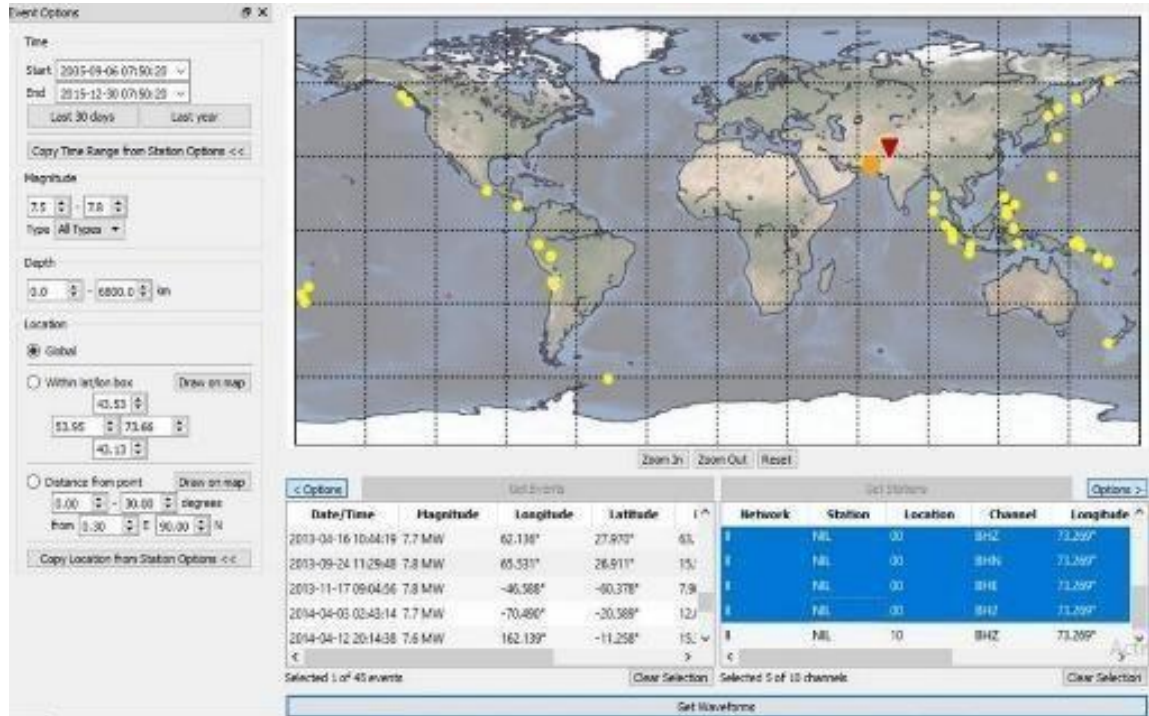


Figure 4. In the figure the orange circle shows the location of September 24th, 2013 Awaran earthquake epicentre, While the red triangle shows the location of the recording NIL station (located in Nilore Islamabad)

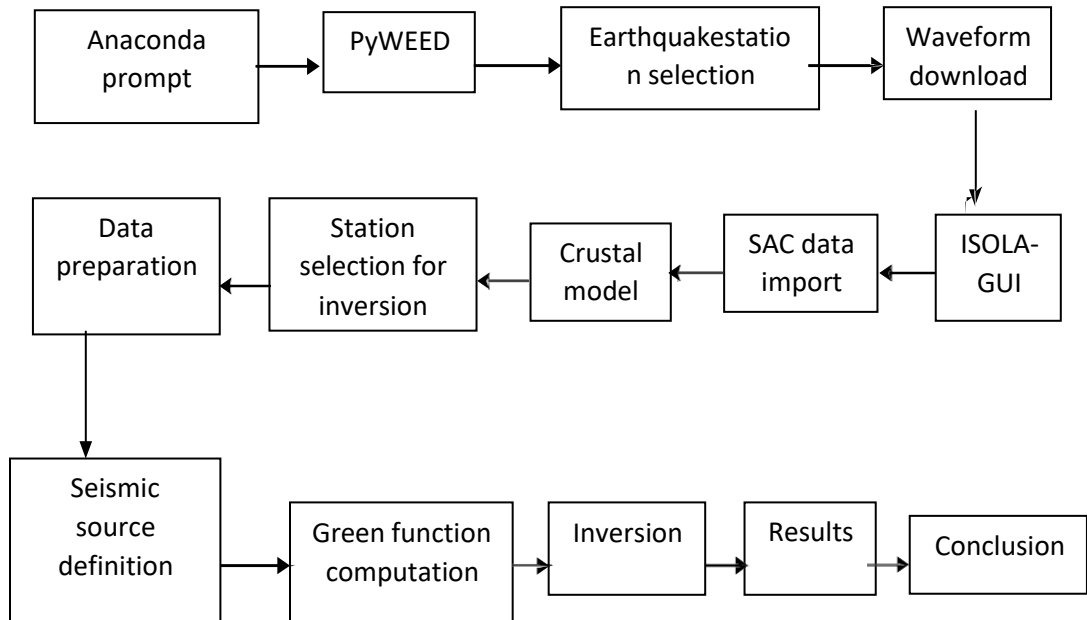
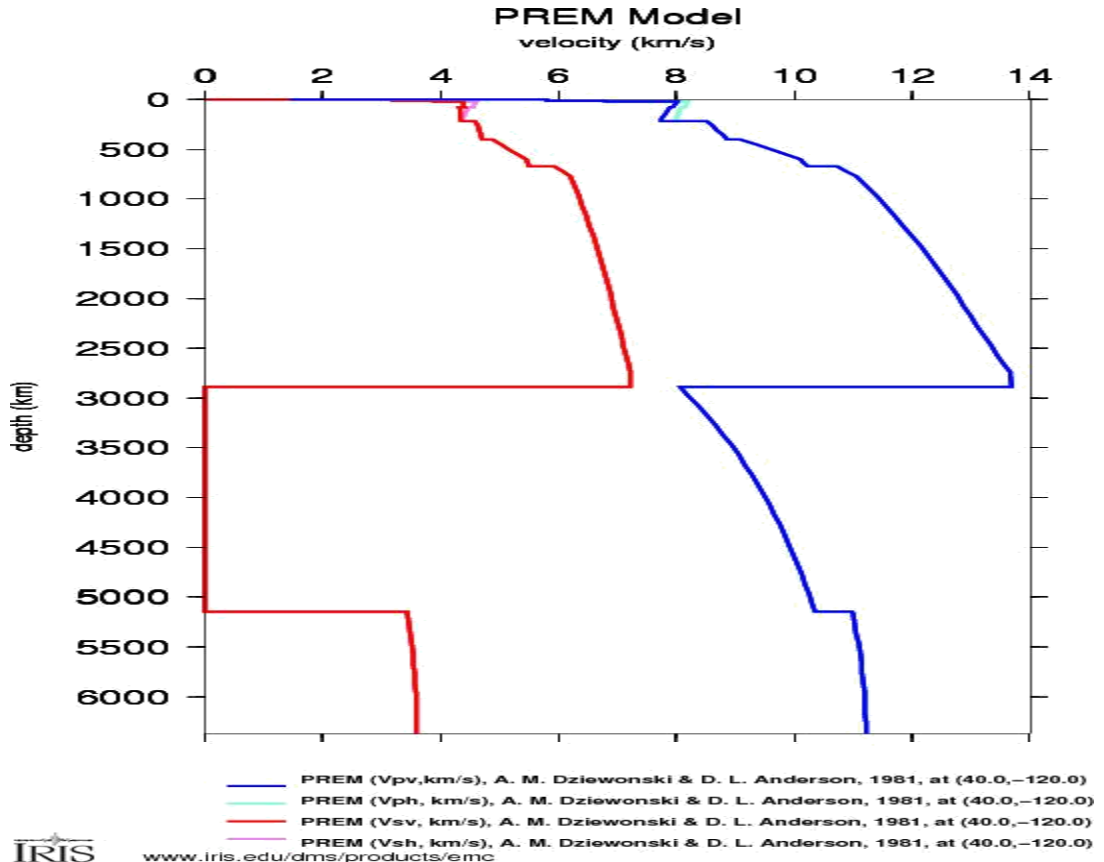


Figure 5. Flow chart of Methodology Adopted for the work

Defining Proper Crustal Model for Earth

ISOLA-GUI operation is a crustal model built with the crustmod tool for all subsequent analysis steps (for example, green function measurement, polarity control, etc.). The vector speeds (V_p and V_s), density, P and S (Q_p and Q_s) are inserted either in text boxes or in text files when the Matlab code provides correct formatting for ISOLA fortran coding. Some devices were available with experimental relationships for generating V_p and V_s velocity graphs with depth and measurement of V and strength. For each season, the symbol supports one cortical model, but future releases support several cortical models. We used the PREM Crustal model to calculate the current tensor for the study period. The main reference earth model (PREM) was 1-D used for seismic experiments on the planet for several years. This model has been developed for various data sets, including free centre oscillation frequency measurements, monitoring of surface waves scattering, travel times for different phases of body waves, radio astronomical data from the field, mass and moment of tranquillity. For our study area, we used 12 layers of the earth's surface (depth 0) to the innercore (6371 km).



www.iris.edu/dms/products/emc

Figure 6. In this PREM Model above the red line shows Vs (Shear wave velocity) and blue line shows the Vp (Primary wave velocity). We notice that from 3000-5200 the Shear wave velocity (Vs) value obtained is zero.

Green Functions Computation

The green function is computed using the wavenumber method. Like coupon delivery, several codes are available remotely to represent data in bullet source or multiple instantaneous tension models. Fortran codes exist as separate executable files called ISOLA- GUI for tasks such as computing and Green reversal. For additional M5 + earthquakes at distances up to 400 km, the code is also proven useful. The overall frequency for our work to measure the green function was 0.1. It was crucial for our results to use such a low frequency in our work, because the attenuation of such lower frequency is not very important. Therefore, the attenuation issue largely doesn't affect our performance.

Spatial Analysis

The primary data of earthquakes was accessed from open source earthquake databases of US Geological Survey and Pakistan Seismic Network of Pakistan Metrological Department. The dataset of 4031 events (spreading over 7 °N to 32° N and 55° E to 71° E) has been self-reviewed and annotated for cataloging. The magnitudes of those events were measured in different scales ranging between 3.7 < m < 8.1. All kinds of magnitude scales

have been translated into unified magnitude scale i.e. moment magnitude (Mw) which is considered most reliable magnitude scale for cataloging. The capabilities of ArcMap tools have been explored for data analysis, clipping and mapping of desired earthquake data. The clipping tools of ArcMap were utilized to select the events within the buffer around a fault line and tectonic lineaments. The clipping tool improve the efficiency in getting data points in response of spatial queries. Since, the primary key of earthquake dataset is the spatial coordinates of epicentre of each event.

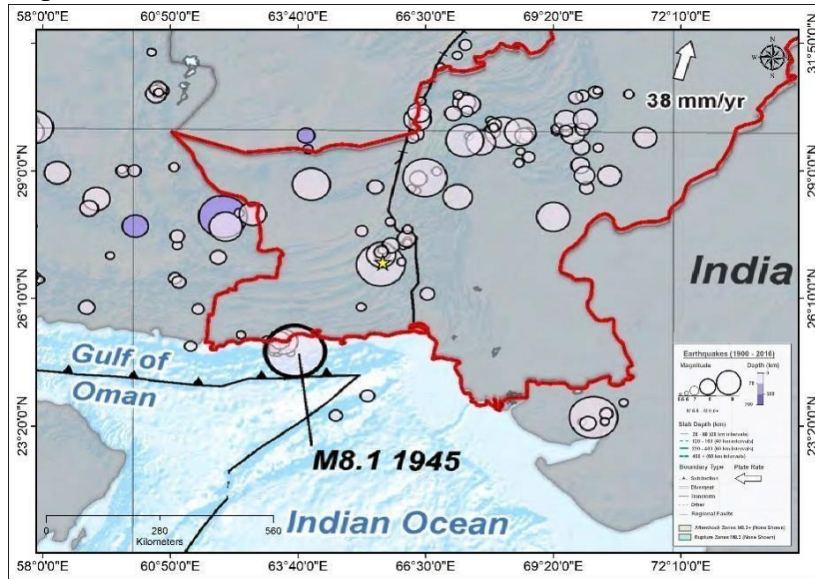


Figure 7: History of Earthquakes from 1900 to 2016

Result and discussion.

This research involves calculating the location and frequency of reflection of the waveform for a test depth in the horizontal source (in the SED position, i.e. in the USGS Focus centre). Fortran ISOLA code is used to revert the Waveform to use speed, while the user interacts even during reflecting in the Mat lab environment. The broad slip of a young failure and an active failure is a riddle about fault geometry's supposed impact on failure dynamics. The seismically active error plans tend to be optimally directed to Anderson's error theory. Slip or slip sources often come out from the axial mechanism of low-cross earthquakes, but slip slipping is relatively rare.. In Fig.8, which shows the stability of the focal length and the best acceptable depth at 17.5 km, the connexion between observations and artificial seismograms is shown in terms of depth. The maximum correlation was found at 0,43 at a depth of 17,5 km and the CC is 100% double. Baluchistan's earthquake highlighted the engineering flaws, preconfigured stress and dynamic vulnerability, as was the case on several previous occasions on the seismic breakage propagation from dynamic modelling.

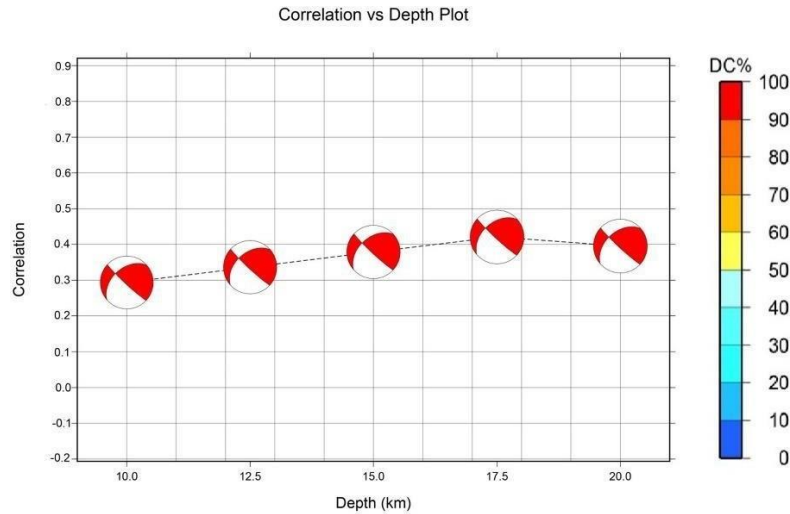


Figure 8: As a function of the test source deepness down the SED focus centre, the correlation between the observed, artificial and focal mechanism waves. DC percent of colors

We determined the earthquake focal mechanism, which equates the USGS strike, sinking and tilt. Then we reverse the seismogram in order to measure the time of launch, the intensity of the earthquake and the tensor's six components. Figures 9 and 10 demonstrate the effects of the reflection. Seismic moment was observed approximately $4,037e + 20$ Nm, the equivalent of Mw 7.7. US Geological Survey has reported the same scale. In contrast to a depth of 15.5 km, the best approach was measured at a depth of 17.5 km. The synthetic seismograms, as shown in the figure, well suit the observations.

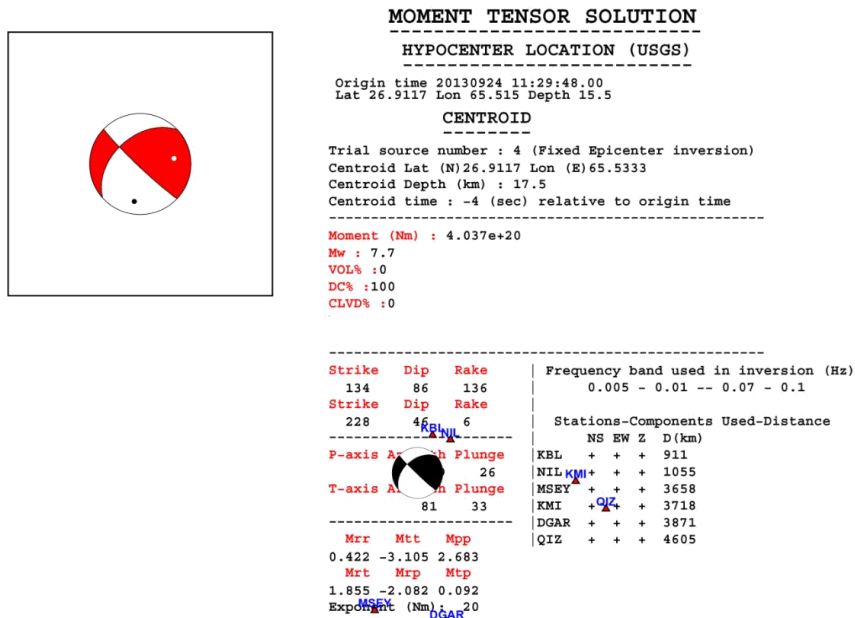


Figure 9. Moment tensor solution of the Awaran earthquake. Triangles show the station used in the inversion.

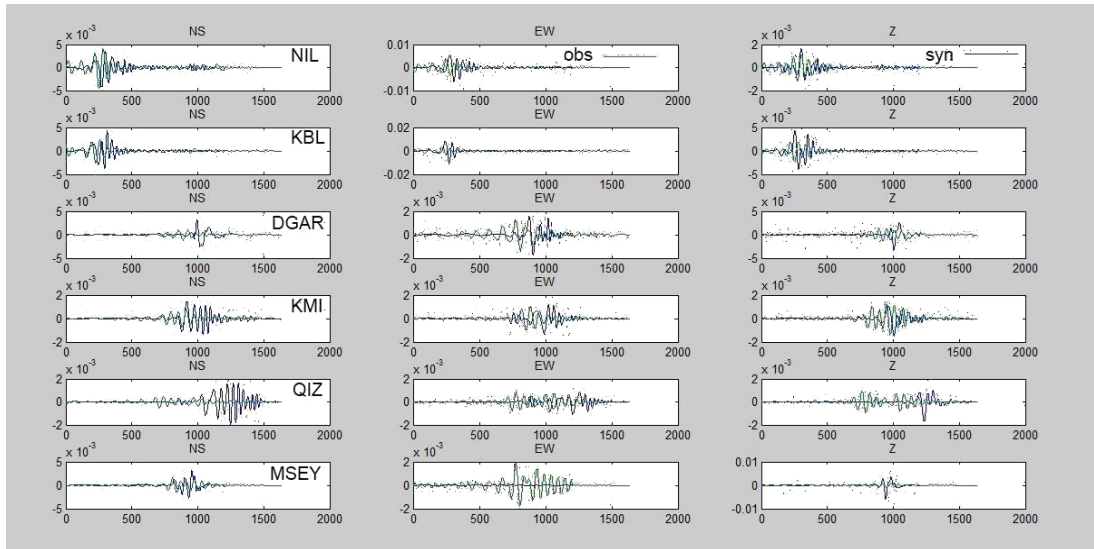


Figure 10. Observed (green line) and synthetic (blue line) velocity (m/s): Frequency ranges 0.005–0.1 Hz, Event 1. Peak amplitudes (in m/s) are on the right-hand side of the figure Since the occurrence of event, the times (in second) are given on the bottom of the plot

Cross-section of Slip Distribution

The strike direction is indicated above each fault plane and the hypocenter location is denoted by a star. Slip amplitude is shown in color and the motion direction of the hanging wall relative to the footwall (rake angle) is indicated with arrows. Contours show the rupture initiation time in seconds.

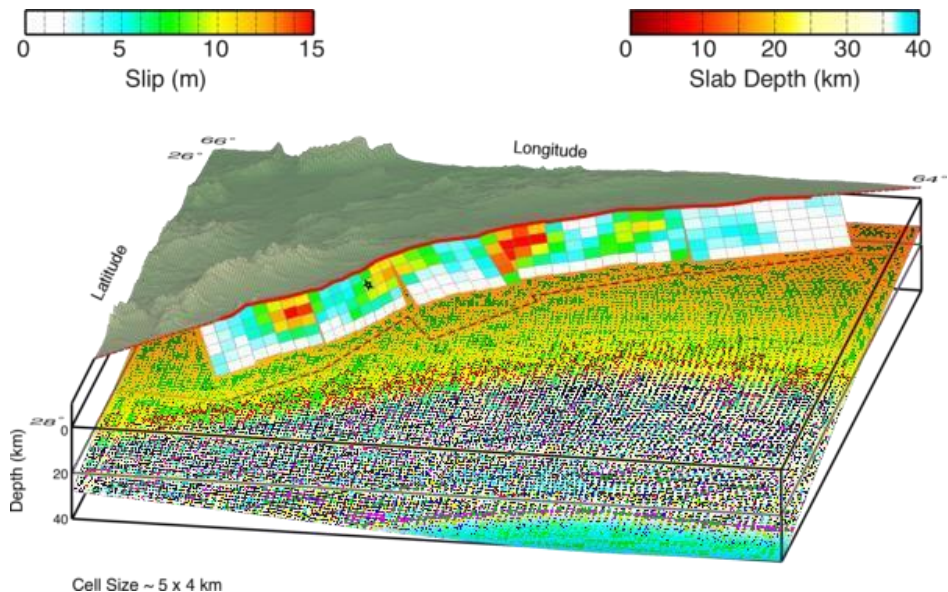


Figure 11. Cross-section of Slip Distribution

Surface projection

Surface projection of the slip distribution was superimposed on GEBCO bathymetry. Thick white lines indicate major plate boundaries [Bird, 2003]. Gray circles, if present, are aftershock locations, sized by magnitude.

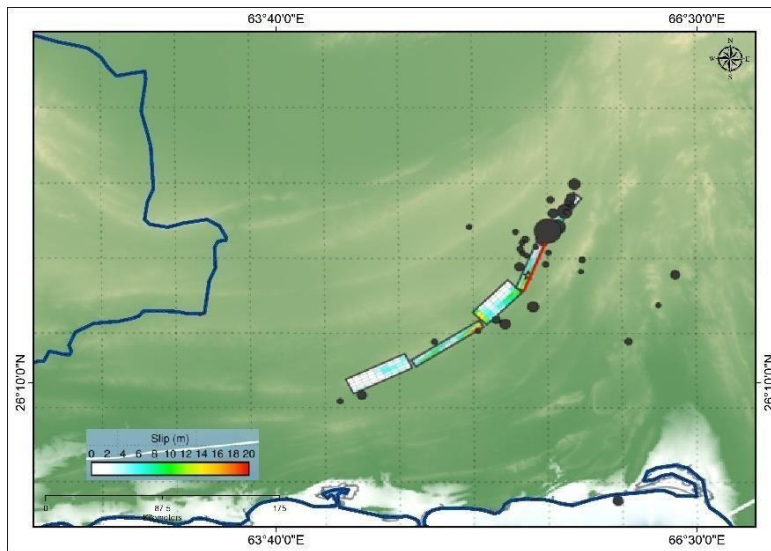


Figure 12. Surface Projection

Spatial analysis of Epicentres of magnitudes

The study area is seismically active, it is diversified in seismogenic potential, earthquake born processes, and consequential variation in magnitude strengths of the earthquakes. The magnitude of earthquakes quantifies the amount of elastic strain energy released during the earthquake. It was revealed that the changes in magnitude strength are not just the statistical data variations, but these changes are closely articulated with the seismo-geological characteristics, deformation and depth of the active fault segments, microseismic proximity to the active margins, structural stability, fault mechanics and its kinematics etc.

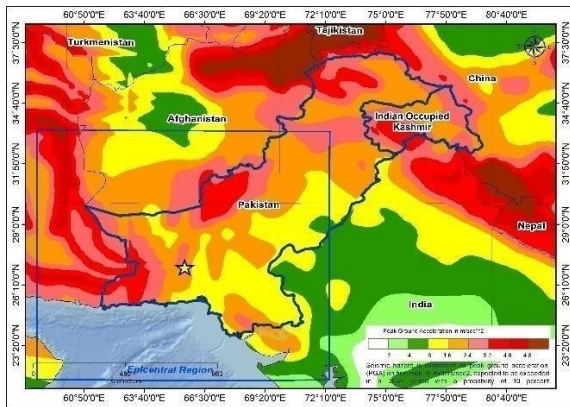


Figure 13. (a) Seismic map of Pakistan

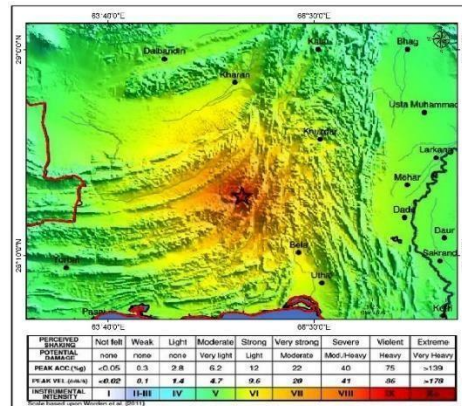


Figure 13. (b) Shakemap of Pakistan

Tectonic Summary

The Awaran earthquake of magnitude, M 7.7 earthquake in south-central Pakistan occurred as a result of oblique strike-slip type at shallow crustal depths. The location, focal mechanism solutions, and finite-fault modeling of the earthquake are consistent with left-lateral (southwest-striking) rupture within the Eurasia plate above the Makran subduction zone. The event occurred within the transition zone between northward subduction of the Arabia plate beneath the Eurasia plate and northward collision of the India plate with the Eurasia plate. The epicenter of the event is 69 km north of Awaran, Pakistan, and in 270 km north of Karachi. On a broad scale, the tectonics of southern and central Pakistan reflect a complex plate boundary where the Indian plate slides northward relative to the Eurasian plate in the east, and the Arabia plate subducts northward beneath the Eurasia plate in the Makran (western Pakistan). These motions typically result in north-south to northeast-southwest strike-slip motion at the location of the September 24th earthquake that is primarily accommodated on the Chaman fault, with the earthquake potentially occurring on one of the southernmost strands of this fault system.

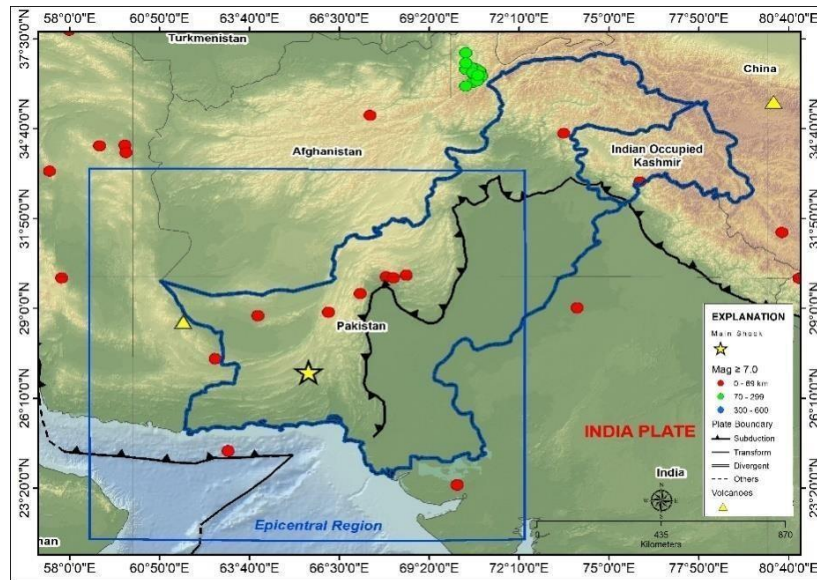


Figure 14. Tectonic map of Pakistan

While commonly plotted as points on maps, earthquakes of this size are more appropriately described as slip over a larger fault area. Strike-slip events are typically about 160x20 km (length x width). Modelling of this earthquake implies dimensions of about 200x20 km, predominantly up-dip and southwest of the hypocentre. Although seismically active, this portion of the Eurasia plate boundary region has not experienced large damaging earthquakes in the recent history.

Conclusion

The data from 6 stations (NIL, KBL, MSEY, KMI, QIZ, DGAR) was used to compute focal mechanisms. By using the low frequencies (0.05-0.1), the problems arising due to attenuation were significantly reduced. The maximum correlation was noticed at 0,43 at a depth of 17,5 km where the CC was 100% double. Baluchistan's earthquake highlighted the engineering flaws, preconfigured stress and dynamic vulnerability, as it was the case on several previous occasions on the seismic breakage propagation from dynamic modelling. The plot of observed waveforms versus synthetic waveforms is well correlated. The use of a standard ground model such as PREM provided a robust focal mechanism. The Mat lab- based graphical user interface makes data management easy, while offering full user control in the workflow and an intuitive graphical overview of the findings. The quantity of DC (double pair) was estimated as 7,7 100%. Today Pakistan is a seismically active and vulnerable to major seismic events. In Pakistan, tectonics needs to be re-invested as a matter of urgency and secret defects found in areas where the population is seriously endangered.

Acknowledgment. The authors would like to thank the anonymous reviewers for their hard work. IRIS, Berkeley University of California and the Institute of Technology have

provided the seismic data used. Open access to these data enables and is widely valued. Source of Parkfield seismic data: U.S. Geological Survey.

Author's Contribution. All authors have contributed equally.

Conflict of interest. The authors declare no conflict of interest in publishing this manuscript in IJIST.

REFERENCES

1. Saifullah.M, Asghar. A, Ahmad.A.M, Zafar.M, Saman.S, Arshad A.M, Akhtar.A. "Computation of Temporal Decline to a Vanished Island (A Case Study Zalzala Koh)". International Journal of Innovations in Science & Technology, Vol 01 Issue 04: pp 142- 150, 2019.
2. Ambraseys, Nicholas, and Roger Bilham. "Earthquakes in Afghanistan", Seismological Research Letters, Vol 74 issue 2, pp: 107–23, 2002
3. Aochi, Hideo, Raul Madariaga, and Eiichi Fukuyama. "Constraint of Fault Parameters Inferred from Nonplanar Fault Modeling." *Geochemistry, Geophysics, Geosystems*, vol4 issue 2 pp: 1–16. 2003.
4. Avouac, Jean Philippe et al. "The 2005, Mw 7.6 Kashmir Earthquake: Sub-Pixel Correlation of ASTER Images and Seismic Waveforms Analysis." *Earth and Planetary Science Letters*, Vol 249, issue 3–4, pp: 514–28, 2006.
5. Barnhart, W. D. et al. "Evidence for Slip Partitioning and Bimodal Slip Behavior on a Single Fault: Surface Slip Characteristics of the 2013 Mw7.7 Balochistan, Pakistan Earthquake." *Earth and Planetary Science Letters*, Vol 420, issue 12, pp: 1–11, 2015.
6. Bilham, Roger et al. "Seismic hazard in Karachi, Pakistan: Uncertain past, uncertain future" *Seismological Research Letters*, Vol 78, issue 6, pp: 601–13, 2007.
7. Bormann, Peter. "Global 1-D Earth Models 1 PREM Model." *Datasheet*, Vol 1, issue 1, pp : 1–12, 2002.
8. Bouchon, Michel. "The Discrete Wave Number Formulation of Boundary Integral Equations and Boundary Element Methods: A Review with Applications to the Simulation of Seismic Wave Propagation in Complex Geological Structures." *Pure and Applied Geophysics*, Vol 148, issue1–2, pp : 3–20, 1996.
9. Buforn, E., C. Sanz de Galdeano, and A. Udías. "Seismotectonics of the Ibero-Maghrebian Region." *Tectonophysics*, Vol 248, issue 3–4, pp: 247–61, 1995.
10. Buland, Ray, and Freeman Gilbert. "Matched filtering for the seismic moment tensors." *Geophysics research letter*, Vol 3, issue 3, pp: 205–206, 1976.
11. Celerier, Bernard. "Seeking Anderson's Faulting in Seismicity: A Centennial Celebration." *Reviews of Geophysics* (2007), Vol 46, issue 4, pp: 1–34, 2008.
12. Dziewonski, Adam M. "Preliminary Reference Earth Model," *Physics of Earth Planet. Interiors*, Vol 25, issue 4, pp: 297–356, 1981.
13. Frohling, E., and W. Szeliga. "GPS Constraints on Interplate Locking within the Makran Subduction Zone." *Geophysical Journal International*, Vol 205, issue 1, pp: 67–76, 2016.

- 14 Isacks, Bryan, and Peter Molnar. "Correction [to 'Distribution of Stresses in the Descending Lithosphere from a Global Survey of Focal-mechanism Solutions of Mantle Earthquakes']." *Reviews of Geophysics* Vol 10, issue 3, pp: 847–847, 1972.
- 15 Kanamori, Hiroo, and Jeffrey W Given. "Use of long-period surface waves for rapid determination Of Earthquake-Source Parameters." *Physics of Earth Planet. Interiors*, Vol 27, issue 1, pp: 8–31, 1981.
- 16 Kikuchi, M, and H Kanamori. "Note on Teleseismic Body-Wave Inversion Program" Earthquake Research Institute, Tokyo University, Japan, pp: 2335–50, 2003.
- 17 Lawrence, R. D. et al. "Thrust and Strike Slip Fault Interaction along the Chaman Transform Zone, Pakistan." *Geological Society Special Publication* Vol 9, issue 1, pp: 363–70, 1981.
- 18 Mahmood, Irfan. "Revisiting major earthquakes in Pakistan." *Geology today*. Vol 31, issue 1, pp: 33–38, 2015.
- 19 McCaffrey, Robert. "Earthquakes and Ophiolite Emplacement in the Molucca Sea Collision Zone, Indonesia." *Tectonics*, Vol 10, issue 2, pp: 433–53, 1991.
- 21 Mokhtari, Mohammad, Ahmad Ala Amjadi, Leila Mahshadnia, and Mandana Rafizadeh. "A Review of the Seismotectonics of the Makran Subduction Zone as a Baseline for Tsunami Hazard Assessments." *Geoscience Letters*, Vol 6, issue 1, pp: 1–9, 2019.
- 22 MonaLisa, and M. Qasim Jan. "Awaran, Pakistan, Earthquake of Mw 7.7 in Makran Accretionary Zone, September 24 2013: Preliminary Seismotectonic Investigations." *Proceedings of the Pakistan Academy of Sciences*, Vol 52, issue 2, pp: 159–68, 2015.
- 24 Oglesby, D. D., and S. M. Day. "Fault Geometry and the Dynamics of the 1999 Chi- Chi, (Taiwan) Earthquake." *Bulletin of the Seismological Society of America*, Vol 91, issue 5, pp : 1099–1111, 2001.
- 26 Patton, Howard. "Determination of Seismic Moment Tensor Using Surface Waves." *Tectonophysics*, Vol 49, issue 3-4, pp: 213–22, 1978.
- 27 Platt, J. P., J. K. Leggett, and S. Alam. "Slip Vectors and Fault Mechanics in the Makran Accretionary Wedge, Southwest Pakistan." *Journal of Geophysical Research* Vol 93, issue 137, pp: 7955–73, 1988.
- 28 Quittmeyer, R.C., and K.H. Jacob. "Historical and Modern Seismicity of Pakistan, Afghanistan, Northwestern India, and Southeastern Iran." *Bulletin of the Seismological Society of America*, Vol 69, issue 3, pp: 773-823, 1979.

- 29 Reilinger, Robert et al. “GPS Constraints on Continental Deformation in the Africa-Arabia-Eurasia Continental Collision Zone and Implications for the Dynamics of Plate Interactions.” *Journal of Geophysical Research: Solid Earth*, Vol 111, issue 5, pp: 1–26, 2006.
- 30 Ritsema, J., and T. Lay. “Long-Period Regional Wave Moment Tensor Inversion for Earthquakes in the Western United States.” *Journal of Geophysical Research*, Vol 100, issue 1, pp: 9853-9864, 1995.
- 31 Sekiguchi, Haruko, Tomotaka Iwata, and Izmit Bay. “Rupture Process of the 1999 Kocaeli , Turkey , Earthquake Estimated from Strong-Motion Waveforms.” (February) , Volume 92, issue 1, pp: 300–311, 2002.
- 32 Sipkin, Stuart A. “Estimation of Earthquake Source Parameters by the Inversion of Waveform Data: Synthetic Waveforms.” *Physics of Earth and planetary interiors*, Vol 30, issue 2-3, pp: 242–59, 1982.
- 33 Sokos, Efthimios N., and Jiri Zahradnik. “ISOLA a Fortran Code and a Matlab GUI to Perform Multiple-Point Source Inversion of Seismic Data.” *Computers and Geosciences*, Vol 34, issue 8, pp: 967–77, 2008.
- 34 Stich, Daniel, Charles J. Ammon, and Jose Morales. “Moment Tensor Solutions for Small and Moderate Earthquakes in the Ibero-Maghreb Region.” *Journal of Geophysical Research: Solid Earth* Vol 108, issue B3, pp: 1-4, 2003.
- 35 Vernant, Ph et al. “Present-Day Crustal Deformation and Plate Kinematics in the Middle East Constrained by GPS Measurements in Iran and Northern Oman.” *Geophysical Journal International* Vol 157, issue 1 pp : 381–98, 2004.
- 36 Wessel, Paul, and Walter H.F. Smith. “Free Software Helps Map and Display Data.” *Eos, Transactions American Geophysical Union* Vol 72, issue 41, pp : 441–46, 1991.
- 38 Wiedicke, M., S. Neben, and V. Spiess. “Mud Volcanoes at the Front of the Makran Accretionary Complex, Pakistan.” *Marine Geology*, Vol 172, issue 1–2, pp: 57–73, 2001.



Copyright © by authors and 50Sea. This work is licensed under Creative Commons Attribution 4.0 International License.